Mechanisms for Organization and Echo Training in a Flash-Flood-Producing Mesoscale Convective System

JOHN M. PETERS AND RUSS S. SCHUMACHER

Department of Atmospheric Science, Colorado State University, Fort Collins, Colorado

ABSTRACT

In this research, a numerical simulation of an observed training line/adjoining stratiform (TL/AS)-type mesoscale convective system (MCS) was used to investigate processes leading to upwind propagation of convection and quasi-stationary behavior. The studied event produced damaging flash flooding near Dubuque, Iowa, on the morning of 28 July 2011.

The simulated convective system well emulated characteristics of the observed system and produced comparable rainfall totals. In the simulation, there were two cold pool–driven convective surges that exited the region where heavy rainfall was produced. Low-level unstable flow, which was initially convectively inhibited, overrode the surface cold pool subsequent to these convective surges, was gradually lifted to the point of saturation, and reignited deep convection. Mechanisms for upstream lifting included persistent large-scale warm air advection, displacement of parcels over the surface cold pool, and an upstream mesolow that formed between 0500 and 1000 UTC.

Convection tended to propagate with the movement of the southeast portion of the outflow boundary, but did not propagate with the southwest outflow boundary. This was explained by the vertical wind shear profile over the depth of the cold pool being favorable (unfavorable) for initiation of new convection along the southeast (southwest) cold pool flank.

A combination of a southward-oriented pressure gradient force in the cold pool and upward transport of opposing southerly flow away from the boundary layer moved the outflow boundary southward. Upward transport of southerly momentum by convection along the southward-moving outflow boundary, along with convectively induced southward pressure gradient forces cut off southerly inflow to the MCS, which temporarily disrupted backbuilding.

1. Background

A large percentage of flash floods in the United States result from heavy convective rainfall associated with specific breeds of mesoscale convective systems (MCSs, on the order of 60%–75%) (e.g., Maddox et al. 1979; Moore et al. 2003; Schumacher and Johnson 2006), where the character of the system's motion results in extended production of heavy rain over a fixed geographic location. "Training" of convection and upstream backbuilding constitute the two predominant mechanisms for heavy rainfall production by MCSs (e.g., Chappell 1986; Corfidi et al. 1996; Doswell et al. 1996; Schumacher and Johnson 2005; Schumacher 2009).

Training involves a convective line in which individual cells predominantly move in the line-parallel direction, resulting in repeated motion of cells over a particular geographic region, while backbuilding involves the repeated geographically fixed upstream (downstream) regeneration (decay) of convective cells, resulting in the convective region of an MCS being quasi stationary. Schumacher and Johnson (2005) termed the two MCS archetypes that most frequently exhibit these behaviors the training line/adjoining stratiform (TL/AS) and backbuilding (BB) archetypes.

The first-order requirement for these phenomena is a continuous supply of the ingredients for moist convection (e.g., Johns and Doswell 1992) to the MCS location by the synoptic-scale environment. This typically constitutes a supply of warm, moist air by the low-level jet with the vertical maxima in convective available potential energy (CAPE) and minima in convective inhibition residing above the surface (hereafter referred to

Corresponding author address: John Peters, Department of Atmospheric Science, Colorado State University, 1371 Campus Delivery, Fort Collins, CO 80521.
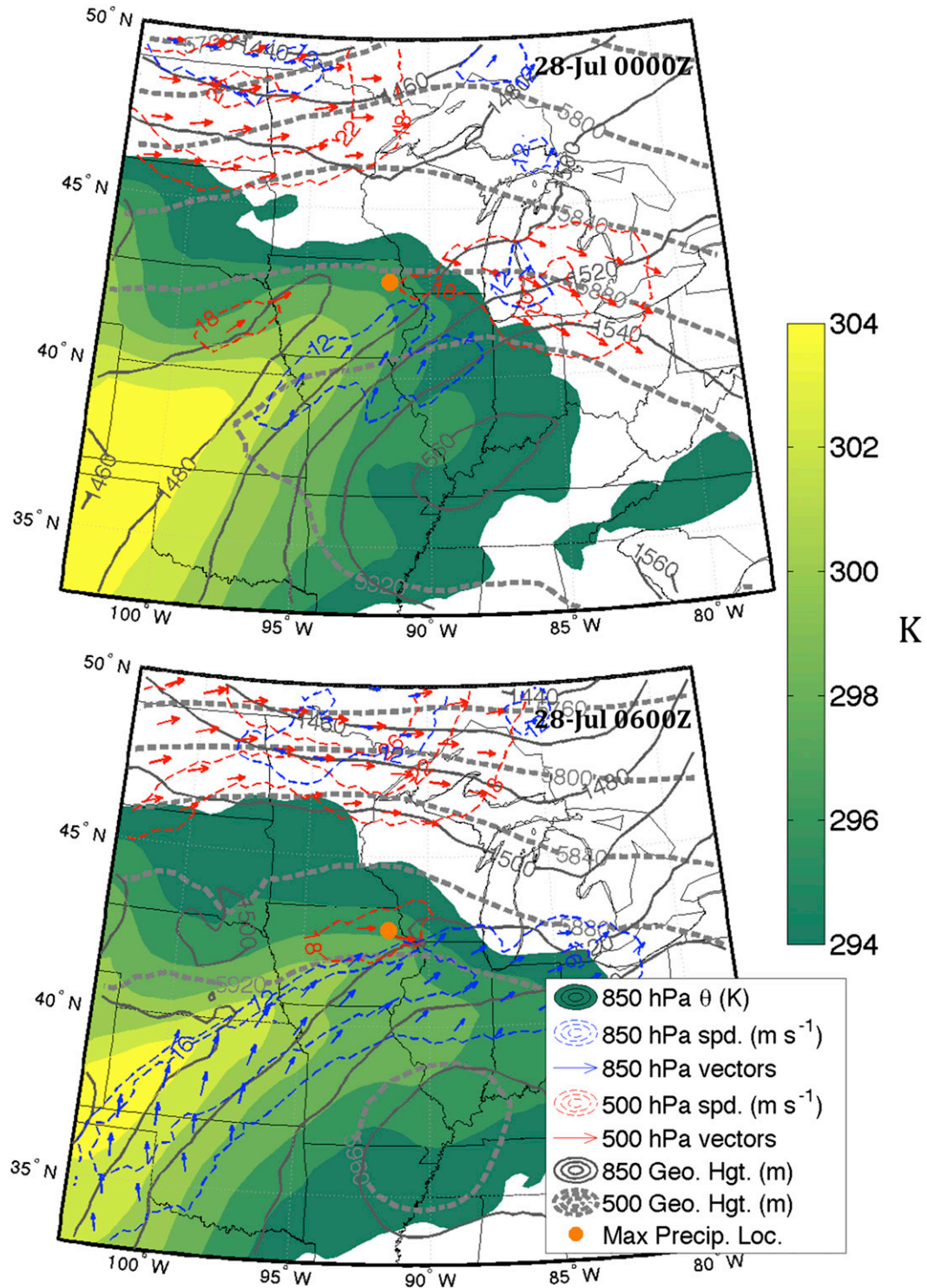E-mail: jpeters3@atmos.colostate.edu

FIG. 1. Regional summary of the atmospheric setup leading to the 28 Jul 2011 TL/AS MCS. Maps were constructed from the NARR. Quantities shown are 850-hPa potential temperature (shading), 850-hPa geopotential height (solid dark gray contours, at intervals of 20 m), 850-hPa wind speed $> 12 \, \mathrm{m \, s^{-1}}$ (dashed blue contours at intervals of $4 \, \mathrm{m \, s^{-1}}$), 850-hPa wind vectors (blue arrows), 500-hPa geopotential height (dashed light gray contours, at intervals of 40 m), 500-hPa wind speed $> 18 \, \mathrm{m \, s^{-1}}$ (dashed red contours, at intervals of $4 \, \mathrm{m \, s^{-1}}$), 500-hPa wind vectors (red arrows), and the location of maximum observed rainfall (orange dot).
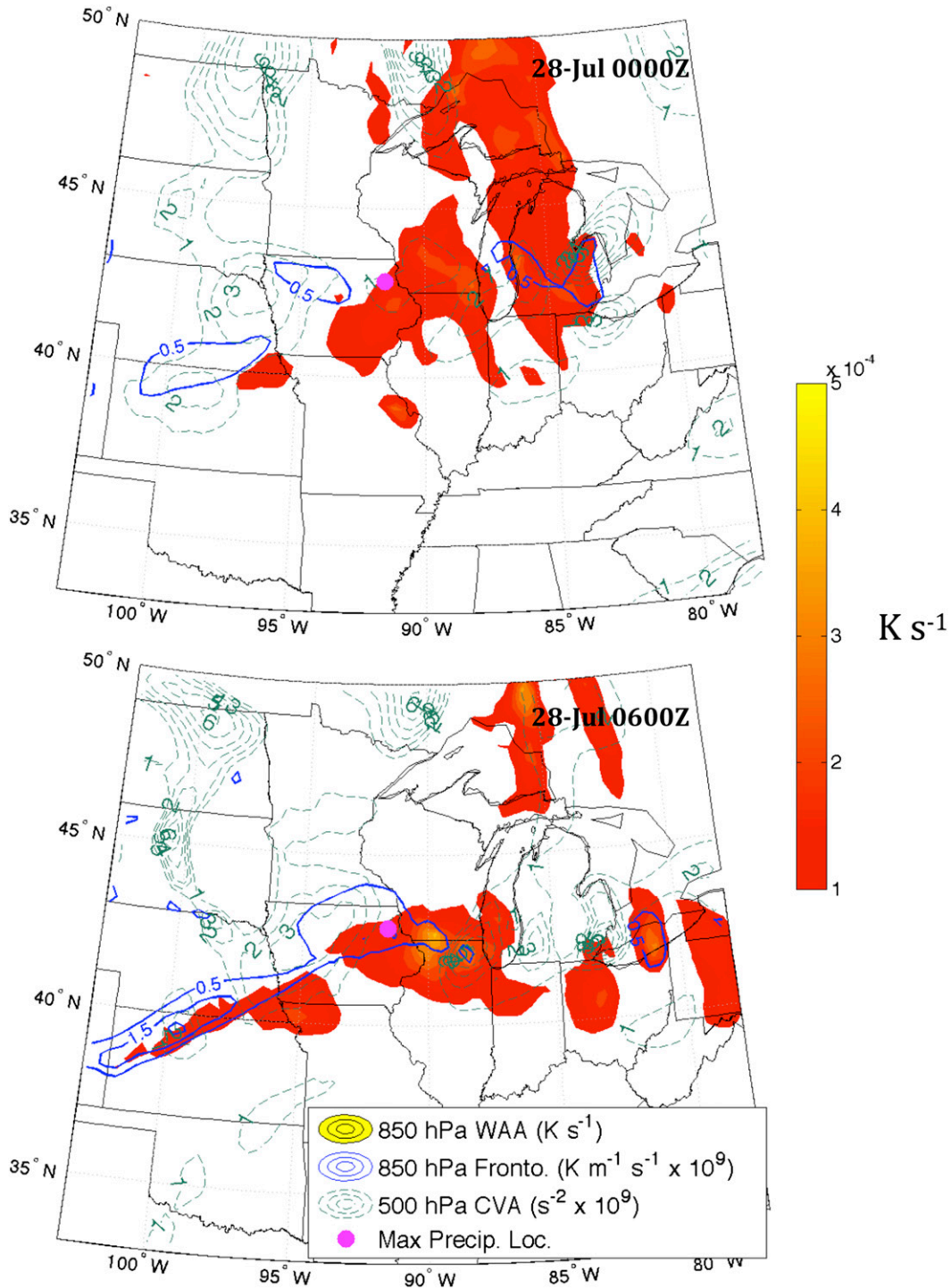
FIG. 2. Summary of the regional large-scale forcing associated with the 28 Jul 2011 TL/AS MCS. Warm air advection (WAA) is shaded, with values below $1 \times 10^{-4}\,\mathrm{K\,s}^{-1}$ removed. Blue contours are horizontal frontogenesis, with a contour interval of $1 \times 10^{-9}\,\mathrm{K\,m}^{-1}\,\mathrm{s}^{-1}$ multiplied by 10^9. Green dashed contours are cyclonic vorticity advection (CVA), with a contour interval of $1 \times 10^{-9}\,\mathrm{s}^{-2}$ multiplied by 10^9. The magenta dot denotes the location where the maximum 1-h precipitation accumulation total was observed.
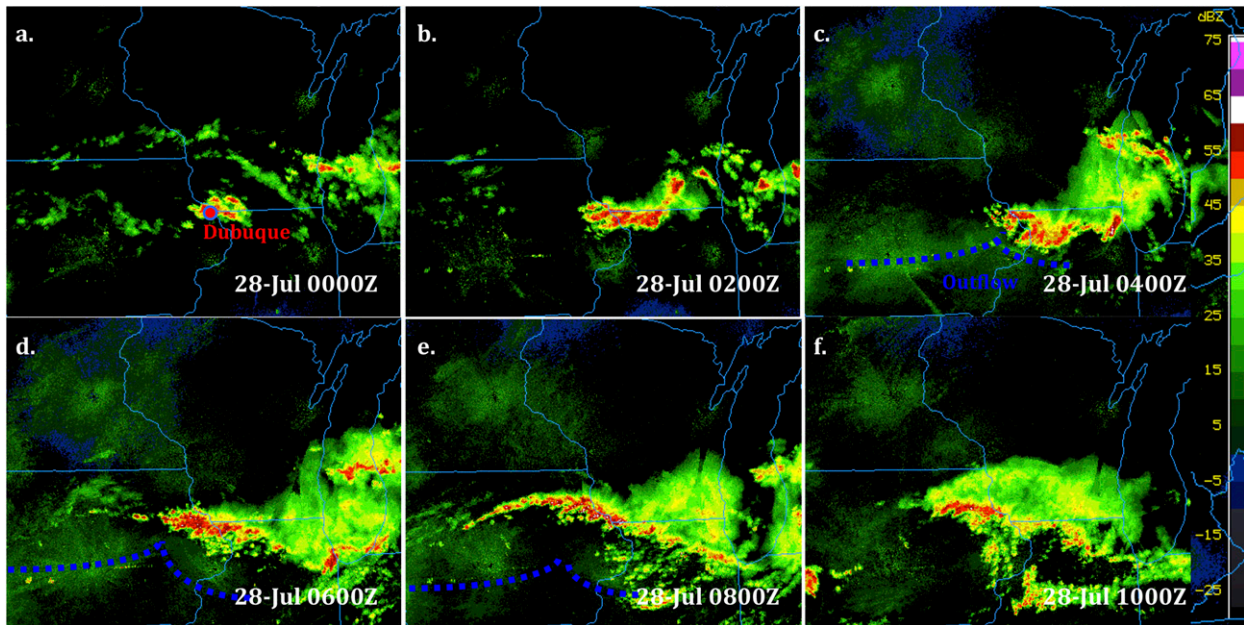
FIG. 3. Observed composite radar reflectivity images (dBZ, shading) from 0000 to 1000 UTC 28 Jul 2011 depicting the evolution of the MCS detailed in this study.

as elevated) (e.g., Moore et al. 2003; Schumacher and Johnson 2006; Wilson and Roberts 2006; Corfidi et al. 2008). Persistent low-level lifting is also often present associated with isentropic upglide and convergence along the nose of a low-level jet (Maddox et al. 1979; Augustine and Caracena 1994; Laing and Fritsch 2000; Moore et al. 2003; Schumacher and Johnson 2005, 2006, 2008; Peters and Schumacher 2014). The factors contributing to the convective-scale organization and evolution of such convective systems, however, remain poorly understood due to their propensity to occur within nocturnal elevated environments, where the well-studied mechanisms for propagation of surface-based convection do not necessarily apply. Furthermore, they are often preceded and/or followed by the passage of a progressive trailing stratiform (TS; Parker and Johnson 2000) MCS (Corfidi 2003; Peters and Schumacher 2014), which undoubtedly influences the local kinematic and thermodynamic environments. In many instances where a training MCS is preceded by a separate progressive MCS, the linear convective region of the training system may be offset from the periphery of the low-level cold pool generated by preceding convection ["bow and arrow effect," Keene and Schumacher (2013); rearward off-boundary development (ROD), Peters and Schumacher (2014)—this phenomenon is described in greater detail in later sections]. Additionally, in the case of quasi-stationary systems, the region of upstream backbuilding often remains stationary for several hours

without obvious orographic influencing factors or a stationary atmospheric boundary (e.g., dryline, outflow boundary) that would intuitively promote such behavior. While previous authors (e.g., Bosart and Sanders 1981; Fritsch et al. 1994; Trier and Davis 2002; Schumacher and Johnson 2008, 2009; Schumacher 2009) show that such instances of quasi-stationary behavior are sometimes explained by the presence of a mesoscale convective vortex (MCV), not all cases involve an obvious MCV. Other potential mechanisms for upstream propagation include standing gravity waves and bores residing along the interface between the stable boundary layer and overlying conditionally unstable air (Crook and Moncrieff 1988; Schmidt and Cotton 1990; Stensrud and Fritsch 1993; Parker 2008; French and Parker 2010; Schumacher and Johnson 2008; Schumacher 2009; Trier et al. 2010, 2011).

This research constitutes the initial phase of a series of numerical modeling experiments that aim to comprehensively address the dynamics of elevated quasi-stationary MCSs—specifically TL/AS systems that occur in the absence of an obvious MCV [since simulations of systems occurring in conjunction with an MCV have been intensively studied by previous works; e.g., Schumacher and Johnson (2008, 2009) and Schumacher (2009)]. The work presented here involves a detailed case study a numerical simulation of an observed flash-flood producing TL/AS event that occurred over Dubuque, Iowa, on 28 July 2011. The evolution of
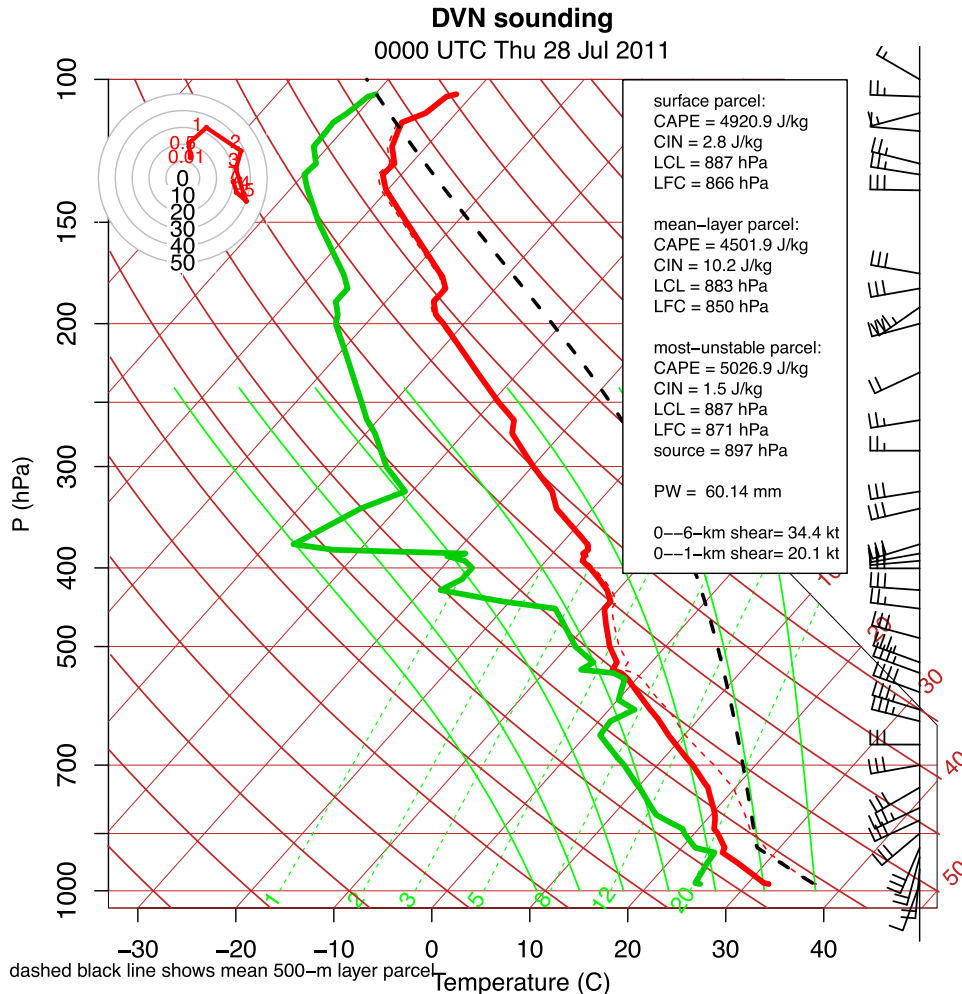
DVN sounding
0000 UTC Thu 28 Jul 2011

FIG. 4. Observed upper-air sounding taken at 0000 UTC 28 Jul 2011 from the Davenport, IA, NWS forecast office.

this system was complex, and featured many of the aforementioned phenomena that frequently occur in the case of quasi-stationary MCSs including preceding/succeeding MCS passages, ROD, and upstream back-building. The organization of this paper is as follows. Section 2 provides an overview of the synoptic-scale setup that led to this event, and describes aspects of the observed radar evolution. Section 3 describes the numerical modeling configuration used to simulate the event, and section 4 outlines characteristics of the simulated MCS, which is dynamically analyzed in section 5. Section 6 summarizes the findings presented here and outlines ongoing and future work.

2. Event overview

A flash-flood-producing TL/AS MCS produced over 150 mm of rainfall accumulation across a large east–west-oriented swath near Dubuque, Iowa, with local rainfall totals as high as 380 mm during the evening of 27 July and early morning hours of 28 July 2011 (National Weather Service Quad Cities Office 2014).

Figures 1 and 2, which show analyzed atmospheric fields from the North American Regional Reanalysis (NARR; Mesinger et al. 2006), summarize the regional atmospheric setup that led to this event. The initial convection associated with the TL/AS MCS developed at roughly 0000 UTC 28 July 2011 along the northwestern periphery of a low-level anticyclone, northern periphery of a southwesterly low-level jet, and beneath a midlevel ridge with weak mid- to upper-level winds (Fig. 1). The region local to the event was characterized by sustained low-level warm air advection fed by a southwesterly low-level jet, along with low-level deformation and corresponding frontogenesis (Figs. 1 and 2). A weak midtropospheric shortwave trough approached
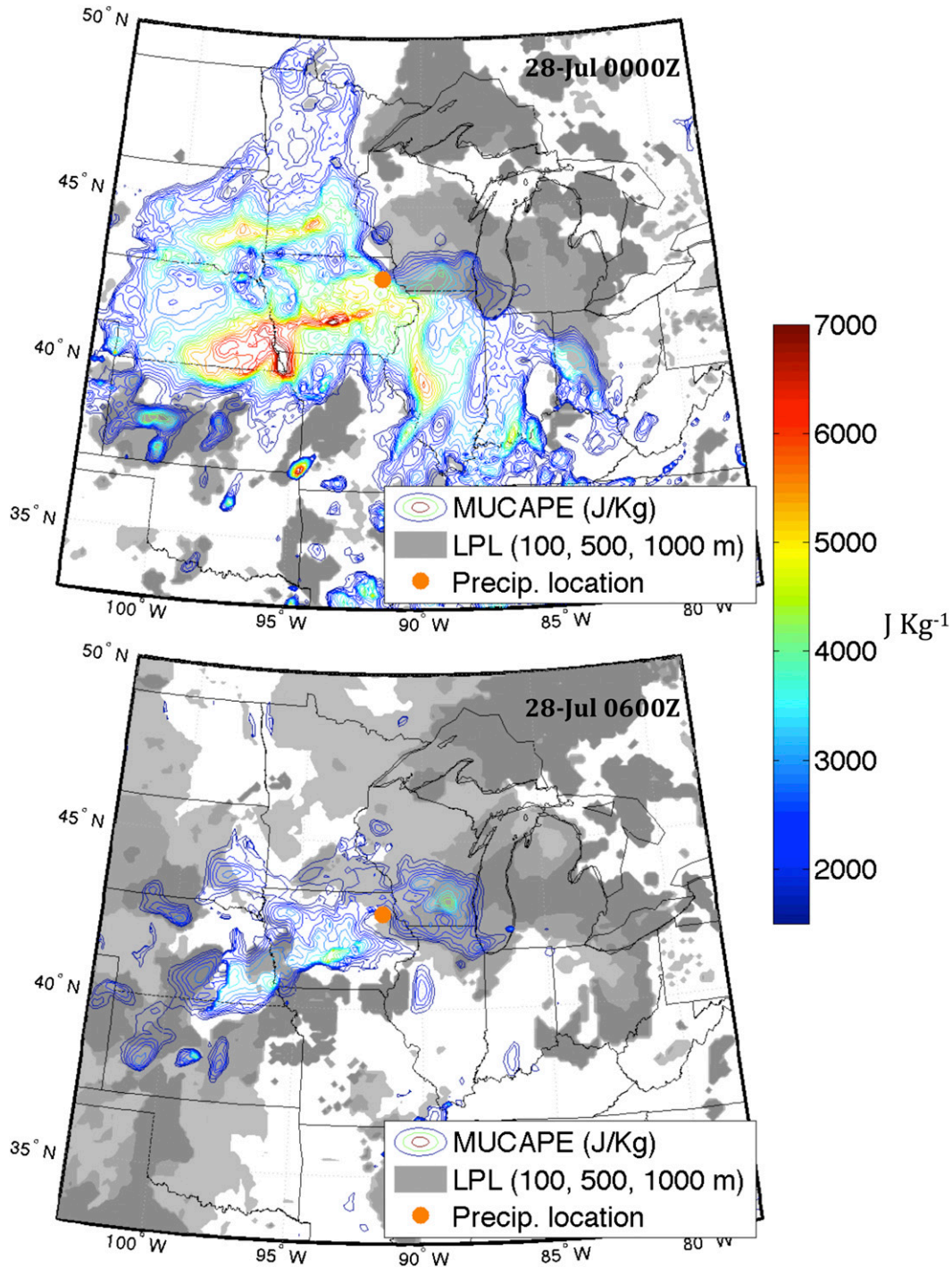
FIG. 5. Analysis of most unstable CAPE (MUCAPE) computed from the Rapid Update Cycle (Benjamin et al. 2004) analysis (color contours, J kg^{-1} at intervals of 100 J kg^{-1}), the height of the maximum CAPE value (m, gray shading at 100-, 500-, and 1000-m increasing increments denoted by increasing darkness of gray shading), and the location of maximum observed rainfall (orange dot) at (top) 0000 and (bottom) 0600 UTC 28 Jul 2011.

the region of interest from the west and contributed to modest cyclonic vorticity advection (CVA; Figs. 1b and 2). This overall synoptic environment was characteristic of the composite TL/AS environment shown by

Schumacher and Johnson (2005), and more specifically the warm-season-type events described by Peters and Schumacher (2014) (contrasted with synoptic-type events, which typically occur in conjunction with stronger flow
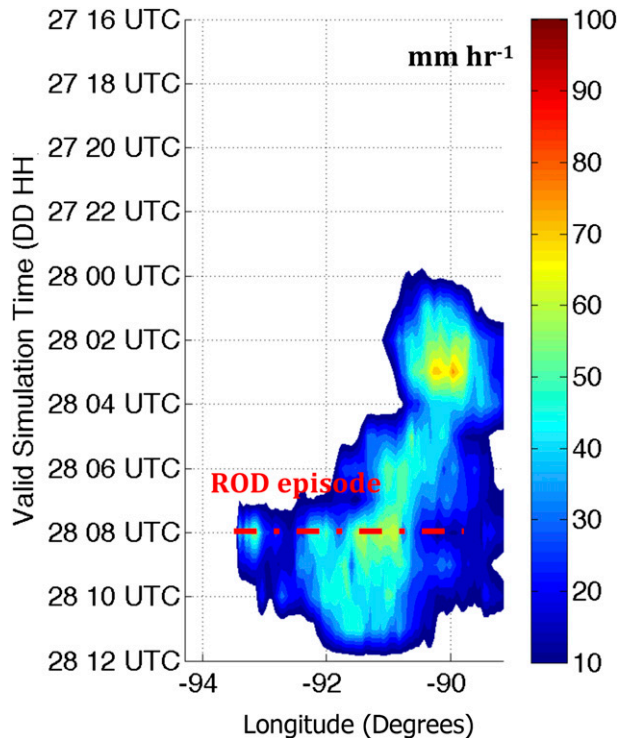
FIG. 6. Hovmöller diagram of the maximum 1-h point precipitation total (mm) in the ST4 analysis within 10 grid points (at a 4-km grid spacing) north or south of each ST4 grid point along a zonally oriented line through the point indicated by the orange dot in Fig. 1 (at approximately 42.5° latitude).
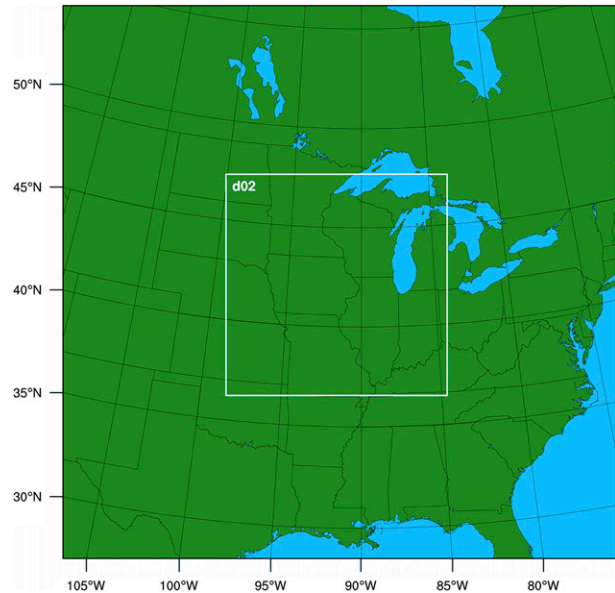

FIG. 7. Locations of both model domains. The periphery of the map denotes the edge of the outer domain, and the white square denotes the edge of the inner domain.

aloft, a stronger low-level cyclone, trailing cold front, and preceding warm front). A fixture of the synoptic-scale setups for such events (including the one studied here) is that the environment provided a *sustained supply* of moisture, instability, and lift (the basic ingredients for deep, moist convection) to the region where heavy rainfall occurred.

A series of composite radar reflectivity images spanning the evolution of this MCS are shown in Fig. 3. Convection initially developed as a multicell cluster of storms near Dubuque at approximately 0000 UTC 28 July (Fig. 3a). These storms organized upscale into a small progressive TS-type MCS that moved eastward and dissipated over northern Illinois (Figs. 3b,c). An observed sounding taken from Davenport, Iowa, at 0000 UTC revealed a highly unstable boundary layer with surface based CAPE (SBCAPE) near 5000 J kg^{-1} (Fig. 4), and maps of NARR-analyzed most unstable CAPE (MUCAPE) showed localized regions of SBCAPE near 6000 J kg^{-1}—these observations suggest the aforementioned first round of thunderstorms was rooted in the planetary boundary layer (PBL). The cold pool produced by this system, along with nocturnal

radiational cooling, then stabilized the PBL and set the stage for subsequent rounds of elevated convective activity (see Fig. 5, where the lifted parcel level near the maximum precipitation location is above the surface by 0600 UTC). In the wake of this initial MCS, an east–west-oriented convective line developed (ROD) and became quasi-stationary, with convection backbuilding to the west of Dubuque and individual convective cells moving predominantly in the convective-line-parallel direction (Figs. 3d–f). ROD is distinguished from other mechanisms for upstream MCS propagation in that a discrete convective line simultaneously redevelops upstream of the initial MCS elevated above the cold pool left by the initial system, and well removed from (usually north of) the surface outflow boundary. Then, following the occurrence of ROD, fixed upstream backbuilding of convection continued along the western end of the line until approximately 1300 UTC 28 July after which the TL/AS MCS weakened and another separate progressive MCS moved through the region (not shown in Fig. 3). The time evolution of precipitation produced by the MCS is summarized in Fig. 6. The most intense observed point-precipitation rates occurred with the first round of convective activity. The ROD episode is also evident as an abrupt westward propagation of the precipitation axis at 0800 UTC (as noted in the figure). This analysis will serve as a means of comparison between the observed MCS evolution and the simulated evolutions that are discussed in the next section.

TABLE 1. List of WRF grid resolutions, grid dimensions, physical parameterizations, and nudging configurations used in this study. Quotation symbols indicate that the parameter is the same as the model configuration in the column to the left. The outer domains for each of the four simulations featured the Grell-3 cumulus parameterization scheme and all other parameters the same as their respective inner domains.

Domain	THOM outer	THOM inner	MORR inner	KESS inner	ERAI inner
Grid spacing	15 km	3 km	" "	" "	" "
Domain dimensions	3000 km × 3000 km	1200 km × 1200 km	" "	" "	" "
Vertical sigma levels	36	36	" "	" "	" "
Model top pressure	100 hPa	" "	" "	" "	" "
ICs and LBCs	NARR	" "	" "	" "	ERA-Interim[a]
Microphysics	Thompson[b]	Thompson[b]	Morrison[c]	Kessler[d]	Thompson[b]
Longwave radiation	RRTM[e]	" "	" "	" "	" "
Shortwave radiation	Dudhia[f]	" "	" "	" "	" "
Surface layer	Eta similarity	" "	" "	" "	" "
Land surface model	NOAA land surface model[g]	" "	" "	" "	" "
Boundary layer physics	MYJ[h]	" "	" "	" "	" "
Cumulus parameterization	Grell-3[i]	None	" "	" "	" "

[a] Dee et al. (2011).
[b] Thompson et al. (2008).
[c] Morrison and Grabowski (2008).
[d] Kessler (1969).
[e] Mlawer et al. (1997).
[f] Dudhia (1989).
[g] Mitchell et al. (2004).
[h] Janjić (1994).
[i] Grell and Dévényi (2002).

3. Model configuration

Version 3.4.1 of the Advanced Research version of the Weather Research and Forecasting (WRF) Model (Klemp et al. 2007; Skamarock et al. 2008) was run with a two-domain nested structure to simulate the 28 July 2011 MCS, with the interface between the two domains configured in one-way mode (i.e., the outer domain provided lateral boundaries to the inner domain only, and no feedback from the inner domain to the outer domain was allowed). The horizontal grid spacing was 15 km for the outer domain, which utilized a convective parameterization scheme, and 3 km for a convection-allowing inner domain. Horizontal domain dimensions were 3000 and 1200 km for the outer and inner domains, respectively, and both domains featured 36 vertical sigma levels (see Fig. 7 for the locations of both domains). All simulations were run from 1200 UTC 27 July to 1200 UTC 29 July 2011 with both domains active through this entire time.

Four simulations were conducted with differing microphysical parameterization schemes and initial and lateral boundary conditions (ICs and LBCs, respectively) as a first-order test of the sensitivity of the simulated MCS evolution to these parameters. A summary of the model parameters used for each simulation is given in Table 1. The NARR was used as ICs and LBCs for three simulations, which featured Thompson microphysics (THOM run), Morrison microphysics (MORR run), and Kessler microphysics (KESS run).

Note that the Kessler microphysics scheme excludes ice physics, and a comparison between the results of this simulation and those employing the more sophisticated schemes provides a first-order assessment of the sensitivity of the convective evolution to ice processes. In the final simulation, ERA-Interim (Dee et al. 2011) was used for ICs and LBCs in place of the NARR with the Thompson microphysics scheme (ERAI run).

The 24-h simulated precipitation accumulation totals from the simulations are compared to observed precipitation in Fig. 8. While the maximum point totals varied between 200 and 300 mm among simulations, which is a slight underprediction, all three NARR-driven simulations produced a large swath of maximized accumulated rainfall displaced approximately 100 km to the southwest of the observed maxima. Interestingly, the ERA-Interim-driven simulation produced a precipitation maxima with a displacement of nearly equal magnitude but of opposite direction (to the northeast). While an investigation of the precise mechanisms that contributed to such biases is beyond the scope of this study, these results suggest that the evolution of the 28 July 2011 MCS exhibited greater sensitivity to synoptic-scale conditions (i.e., ICs and LBCs) than internal convective processes. This result is supported by the work of Peters and Roebber (2014), who showed that a large percentage of the variance in modeled placement of heavy precipitation produced by TL/AS systems was explained by uncertainty in synoptic-scale atmospheric conditions.
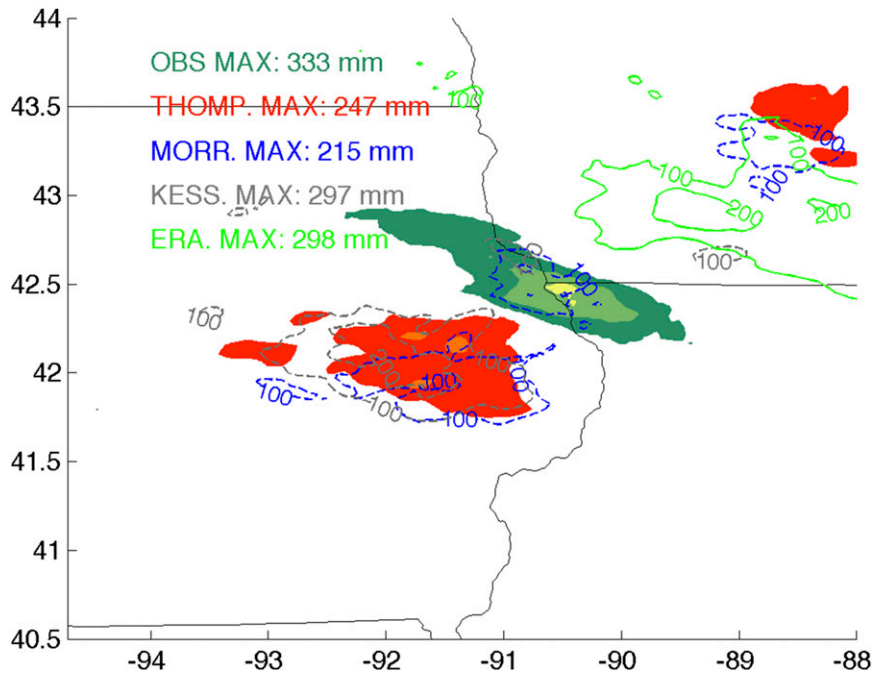
FIG. 8. Comparison of the ST4 24-h accumulated precipitation analysis ending at 1200 UTC 28 Jul 2011 (green shading at intervals of 100 mm, lighter colors indicate greater totals) to modeled accumulated precipitation totals over the same time frame from the THOM (red shading at intervals of 100 mm, lighter colors indicate greater totals), MORR (dashed blue contours at intervals of 100 mm), KESS (dashed gray contours at intervals of 100 mm), and ERAI (solid green contours at intervals of 100 mm) simulations.

Figure 9, which summarizes the time evolution of precipitation in the simulations, facilitates further comparison between the simulations and observations. The NARR-driven simulated MCSs underwent two distinct ROD episodes (only one occurred in observations): one at approximately 0400 UTC and a second at 0700 UTC, which is a potential explanation for the slightly lower modeled accumulated precipitation values relative to observations (i.e., the cold pool surges resulted in convection briefly exiting the region of heaviest rainfall accumulation). These events are evident in Fig. 10, which shows representative simulated radar reflectivity images from the THOM run. The ERA-Interim-driven simulated MCS, however, did not exhibit a coherent ROD episode (though back-building convection did gradually propagate upstream, and the system remained elevated over a cold pool). Our subjective analysis of simulated reflectivity indicated that each of the NARR-driven simulations reproduced the salient radar-observed features of the observed MCS remarkably well, with the timing of convective initiation associated with the TL/AS and dissipation of the system approximately an hour delayed in the model. The characteristics of the simulated radar reflectivity from the ERA-Interim-driven simulation (not shown), on the

other hand, were noticeably different from observations and the NARR-driven simulations.

The THOM run overall best mimicked the observed evolution of the MCS in simulated reflectivity and featured a more complete microphysics package than the KESS run (which produced a closer maximum precipitation total to OBS, but may have done so for the "wrong reasons," owing to the absence of ice phase in the microphysics scheme). We, therefore, chose to concentrate our dynamical analysis of the evolution of this event on output from the THOM run as a proxy for high-resolution four-dimensional observations of the environment (which are unavailable for this event). As a supplementary check of the similarity between our simulation and observed MCS, we compared maps of analyzed atmospheric fields from the Storm Prediction Center (SPC) National Sector Mesoanalysis Archive (not shown) to the analogous fields produced by our model simulation, and found the overall evolution of these fields to be similar.

Finally, in order to test the sensitivity of the convective evolution to horizontal and vertical grid spacing, an additional simulation was conducted with a third 1-km inner nest centered at the MCS location, 50 vertical levels (increased from 36 in the other four simulations),
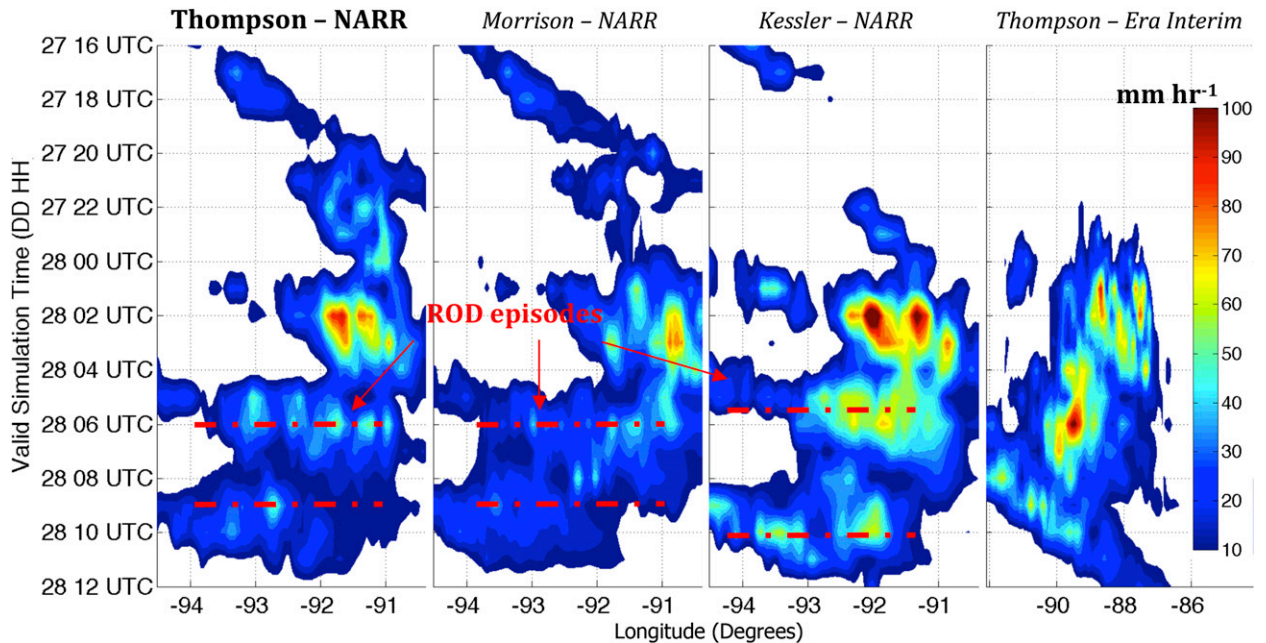
FIG. 9. Hovmöller diagrams of the maximum 1-h point precipitation total (mm) for (left to right) four different model simulations within 15 grid points (at a 3-km grid spacing) north or south of each model grid point along a zonally oriented line at approximately 42° latitude for the NARR-driven simulations, and 43°N for the ERA-Interim-driven simulation.

and all other attributes the same as the THOM run. The subjective evolution of the MCS on both the 3-km and 1-km domains in this run remained very similar to that of the THOM run. While a substantially finer horizontal resolution than that afforded by 3-km (and even 1 km) grid spacings is required to resolve the dynamics of individual convective updrafts (Bryan et al. 2003), the horizontal grid spacing used here has been shown in previous studies (e.g., Weisman et al. 1997; Schwartz et al. 2009) to emulate MCS-scale processes. Since the focus of this study will be to assess the dynamics of MCS-scale processes and their influence on the convective system of interest (which occur on the order of 10–100 km), the lower effective resolution threshold of our grid spacing ($\sim$7 dx, or $\sim$20 km) is sufficient here, deeming the computational expense of analyzing the 1-km simulation unnecessary.

4. Characteristics of the simulated MCS

a. Kinematic and thermodynamic structures

Figure 11 shows snapshots from the time evolution of surface winds and potential temperature perturbations θ', computed by subtracting the full θ field from a Barnes's filtered θ field with a radius of influence of 150 km (see Barnes 1964). The results of the Barnes's filtering processes were found to be insensitivity to small changes in the magnitude of this parameter, and a value of 150 km was subjectively determined to isolate synoptic-scale wavelengths from the features produced by the convective system. A surface cold pool was evident throughout the evolution of the MCS, with the cold pool expanse and intensity having been maximized at 0300 (Fig. 11a) and 0700 UTC (Fig. 11c). Local neutral-to-warm anomalies were also present within the cold pool (especially evident in Figs. 12b,d)—features that have been observed in previous studies of elevated convective systems with cold pools (e.g., Schumacher 2009). The component of flow within the cold pool orthogonal to the outflow boundary along the southwestern periphery of the system was strongest at 0300 and 0700 UTC, which illustrates that the southward movement of this boundary during these times (0300 and 0700 UTC were during the first and second cold pool surges, respectively). Conversely, the southwestern outflow boundary was ill defined at 0500 UTC, and the outflow boundary normal wind component within the cold pool along the southwest flank was weak at 0900 UTC.

The analogous quantities to those shown in Fig. 11 are shown in Fig. 12 for the eighth model sigma level, corresponding to approximately the 820-hPa surface. While a cold anomaly was still evident along the southeast periphery of this system at this level (Figs. 12a,b), unmodified sigma 8 flow rose over the surface cold pool along the southwest periphery of the system and directly
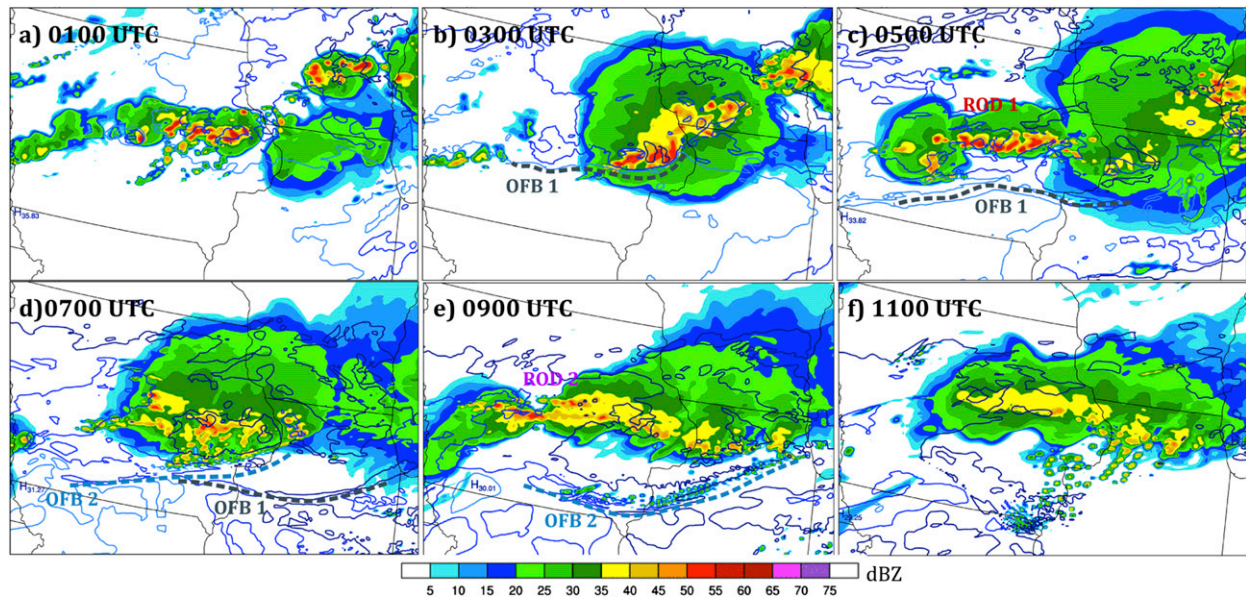
FIG. 10. Simulated radar reflectivity images (shading, dBZ) of the modeled MCS from 0100 to 1100 UTC 28 Jul 2011. Surface temperature contours of 25°, 27°, and 29°C are dark blue, blue, and light blue contours, respectively.

entered the region where ROD occurred between 0400 and 0500 UTC (Fig. 12b—shown in greater detail in section 4b). The effect of the west–east passage of convection on the sigma 8 flow field was to induce a considerable westerly flow component at ~41.75°N (Fig. 12c), as well as to generate a zonally oriented horizontally confluent flow pattern to the west of the system. This zonally oriented confluence served as a potential linear organizational mechanism for subsequent rounds of upstream (relative to the progressive MCS segment) convective activity.

Figure 13 shows a 4-h time evolution (0100–0400 UTC) of CAPE and convergence on the eighth model level that temporally encompassed the first ROD episode. As the initial grouping of convective cells progressed from west to east between 0100 (Fig. 13a) and 0200 UTC (Fig. 13b), CAPE values to the rear of the system north of the surface cold pool boundary were near zero (having been presumably stabilized by convective overturning). Between 0300 (Fig. 13c) and 0400 UTC (Fig. 13d), however, southwesterly flow overran the surface cold pool boundary to the rear of the system and CAPE here increased substantially, eventually leading to new convective development in this region (ROD) by 0400 UTC (Fig. 13d, we will hereafter refer to these CAPE resurgence periods as "return flow" episodes). Prior to ROD and within the wake of the 0100–0200 UTC (Figs. 13a,b) progressive MCS, a well-defined east–west-oriented convergence band developed at 0300 UTC at roughly 42.2°N (Fig. 13c), within which new convective

cells eventually developed. Figure 14 provides evidence that the source of "CAPE revitalization" in the MCS upstream wake region just prior to ROD was a result of high θ_e air ("high θ_e" refers to a local maximum in the vertical distribution of this quantity) being transported up and over the surface cold pool by southwesterly flow (Fig. 13). Two outflow boundaries (OFBs) are evident at 0200 and 0230 UTC (notated in Figs. 14a,b), with OFB 1 presumably having been generated by convection prior to the 0000 UTC round of convective activity that marked the onset of the studied MCS, and OFB 2 having been left between 0000 and 0200 UTC by the first progressive convective surge associated with the studied MCS. The maximum θ_e at 0200 UTC (Fig. 14a) and minimum in convective inhibition (CIN) within the cross section resided near OFB 1 [~(41.3°–41.7°N)]. A region of lifting along, and localized to OFB 1 is also evident at approximately 41.3°N (Figs. 14a,b). Between 0230 and 0330 UTC (Figs. 14b–d), the maximum θ_e shifted northward above the cold pool boundary into the 41.8°–42.2°N range. CIN gradually eroded near the maximum θ_e values during this time frame, and had approached zero throughout the entire vertical column near 42.1°N (this is where a new convective updraft initiated approximately 10 min later). The horizontal extent of lifting in the north–south direction also expanded during this time frame, and there was arguably enhanced lifting over the enhanced low θ_e region north of OFB 2, suggesting that gradual lifting over the cold pool played a role in eroding CIN.
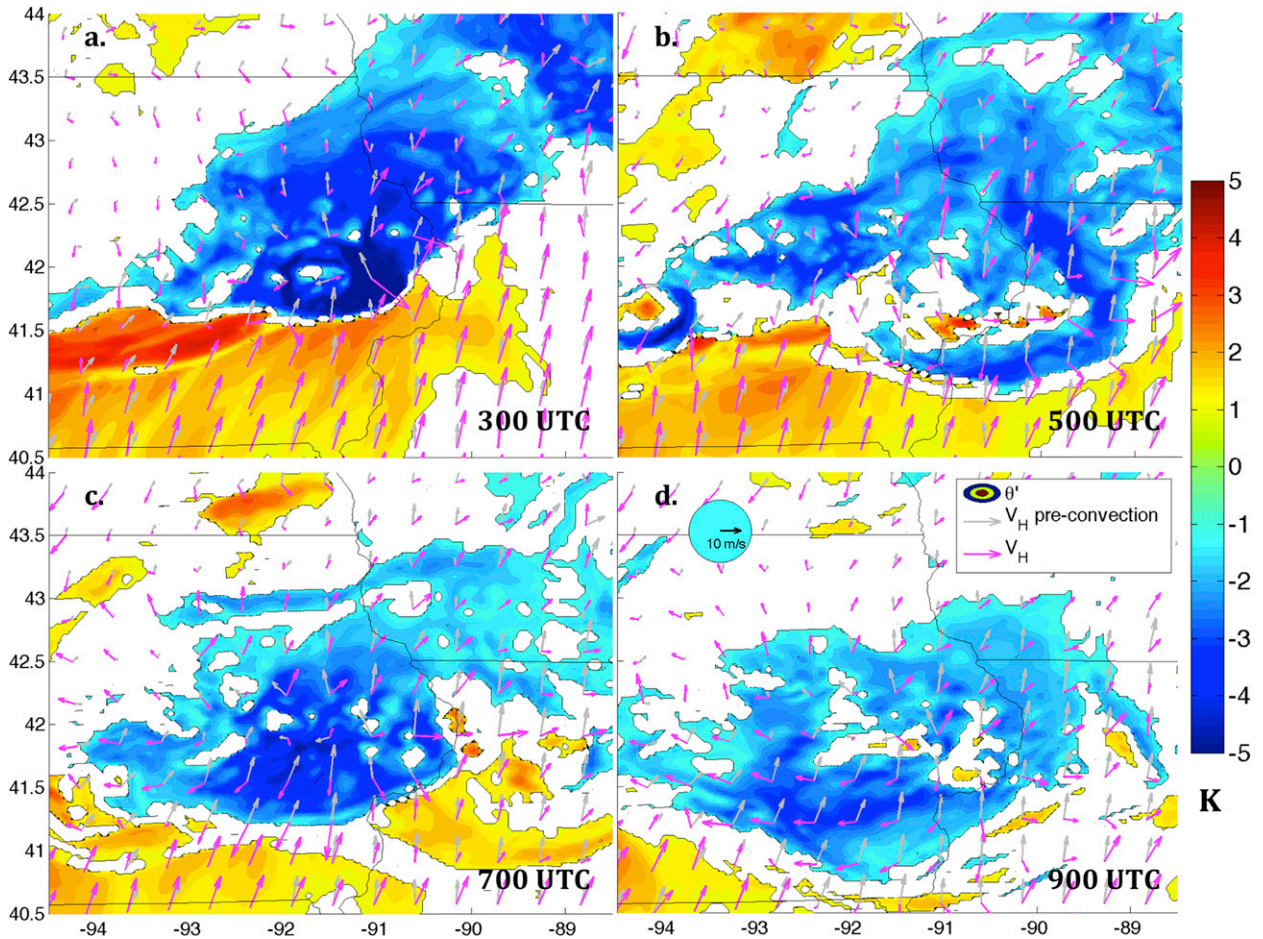
FIG. 11. Perturbation potential temperature (θ') on the first model sigma level (shading, K), wind vectors on the first model sigma level at the valid time indicated in each panel (magenta arrows, m s^{-1}), and wind vectors on the first model sigma level at 2300 UTC 27 Jul 2011 (gray arrows, m s^{-1}; included to illustrate the change in wind between 2300 UTC and the valid time in each frame).

An upward arch in isentropes near OFB 1 was evident during the 0200–0230 UTC time frame (Figs. 15a,b), which reflects dynamically forced adiabatic ascent and descent as flow passes the outflow boundary. This lift was apparently insufficient to trigger deep convection, perhaps due to the 3000–4000-m layer remaining convectively inhibited (Figs. 14a,b). The north–south prevalence of low-level warm-air advection (WAA) increased between 0230 and 0300 UTC (Figs. 15b,c) as the southeasterly low-level jet reentered the region that was affected by the progressive MCS (this is evident in Fig. 13, and discussed in greater detail in section 5b). WAA spanned the entire north–south extent of the cross section including regions south of the surface outflow boundary, suggesting that there was a large-scale contribution to this process in addition to enhanced lifting over the cold pool. A region of saturation at ~2000 m expanded between 0300 and 0330 UTC (Figs. 14c,d), which is the region where ROD convection eventually developed. Figures 14

and 15 suggest that the northward separation of ROD convection from the OFB(s) was regulated by the time (and horizontal distance) required for air to reach saturation and erode convective inhibition through the entire lower troposphere.

Sets of back trajectories were initialized within two separate updrafts within ROD convection to the rear of the first progressive MCS segment—one updraft at 0350 UTC and another at 0400 UTC—with both trajectory sets having been initialized 10 min after the first appearance of vertical velocity exceeding 1 m s^{-1} associated with the updraft. The horizontal and vertical paths of these trajectories are shown in Fig. 16. Air parcels originated within southwesterly low-level return flow and remained elevated in the 3 h prior to their initialization. Their paths shortly prior to their entry into convective updrafts coincided with vertical maxima in CAPE (Figs. 16c,d). There is evidence of initial vertical oscillations of air parcels, which presumably occurred as they interacted with the
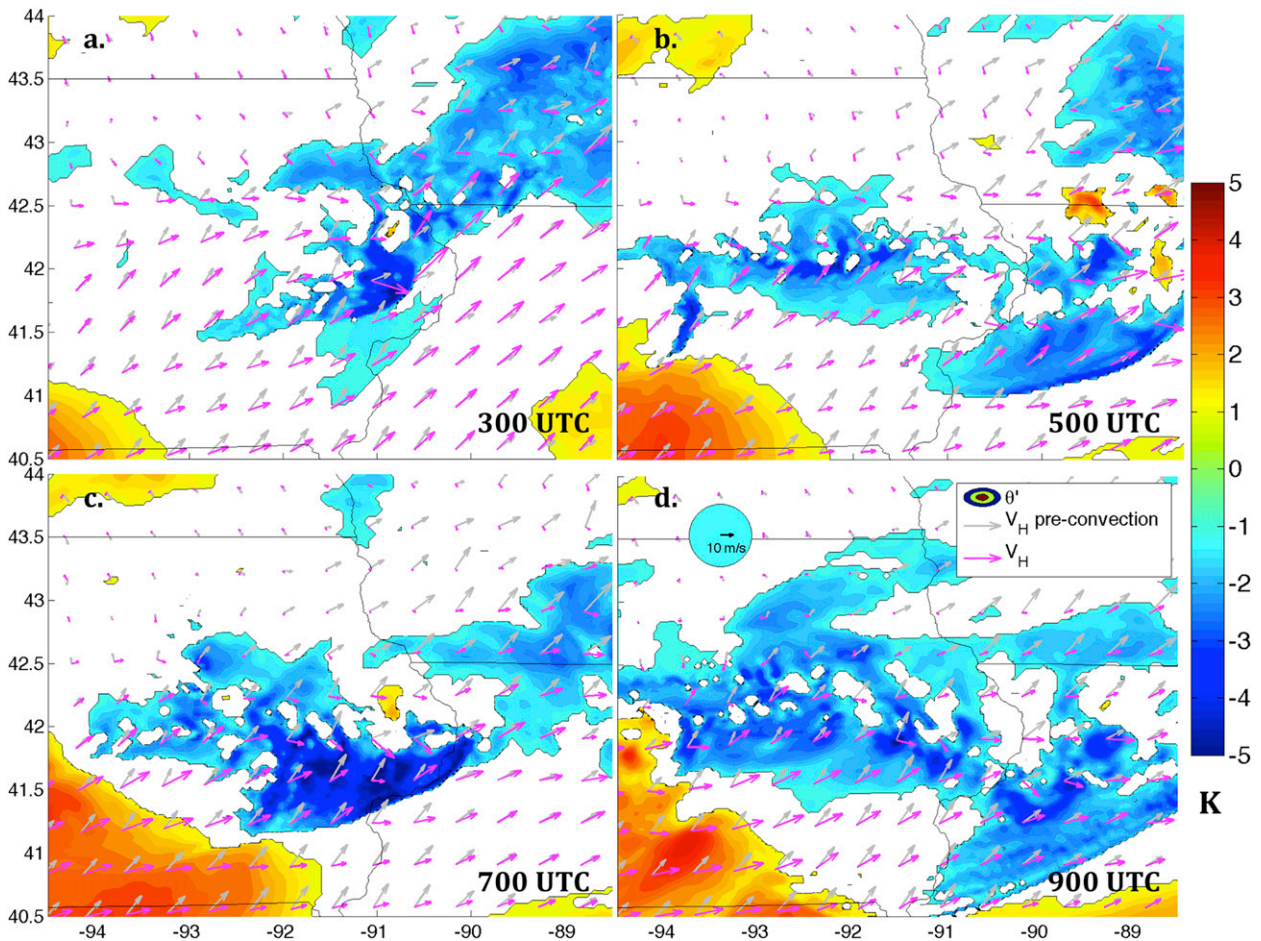
FIG. 12. As in Fig. 11, but for the eighth model sigma level. The average pressure on this level was roughly 820 hPa.

southern periphery of the surface cold pool. All air parcels then experienced gradual lifting for roughly an hour before entering convective updrafts, during which they ascended 500–1000 m from their lowest positions. Figure 17, which depicts diagnostic quantities along the trajectory paths, shows that the gradual ascent that occurred prior to convective onset coincided with initial cooling of the air parcel relative to its surroundings (evident in negative T' values), along with gradually increasing relative humidity. The coincidence of increasing relative humidity, negative T' (presumably due to adiabatic cooling), and prolonged gradual ascending motion corroborates our earlier assertion that layer lifting was locally enhanced near the convection (perhaps resulting from lifting over the cold pool). This gradual lifting echoes the results of Trier et al. (2010, their Fig. 18b) in a similar backbuilding MCS, as well as the trajectory results of Keene and Schumacher (2013) and Trier et al. (2014)'s calculations of parcel buoyancy for elevated MCSs.

b. Vertical wind shear along the outflow boundary

Previous authors have demonstrated that horizontal variations in the outflow-boundary-relative environmental wind shear orientation along the flanks of a cold pool explain asymmetries in the system's structure (e.g., Rotunno et al. 1988; Corfidi 2003; Parker 2007; French and Parker 2010; Weisman and Rotunno 2004). Rotunno et al. (1988) showed that in many cases of linear MCSs, the ratio $C/\Delta U$ explains the optimality for vertically upright updrafts along the outflow boundary, where C is the cold pool velocity and ΔU is the magnitude of the vertical wind shear in the warm buoyant air adjacent to the cold pool, over the depth of the cold pool. Specifically, $C/\Delta U \approx 1$ corresponds to a robust kinematically forced vertical jet along the cold pool edge, which may easily lift parcels with nonzero CAPE to their levels of free convection (LFCs). Ratios much smaller (larger) than 1 result in weaker upshear (downshear) tilted lofting of air parcels, and lifting
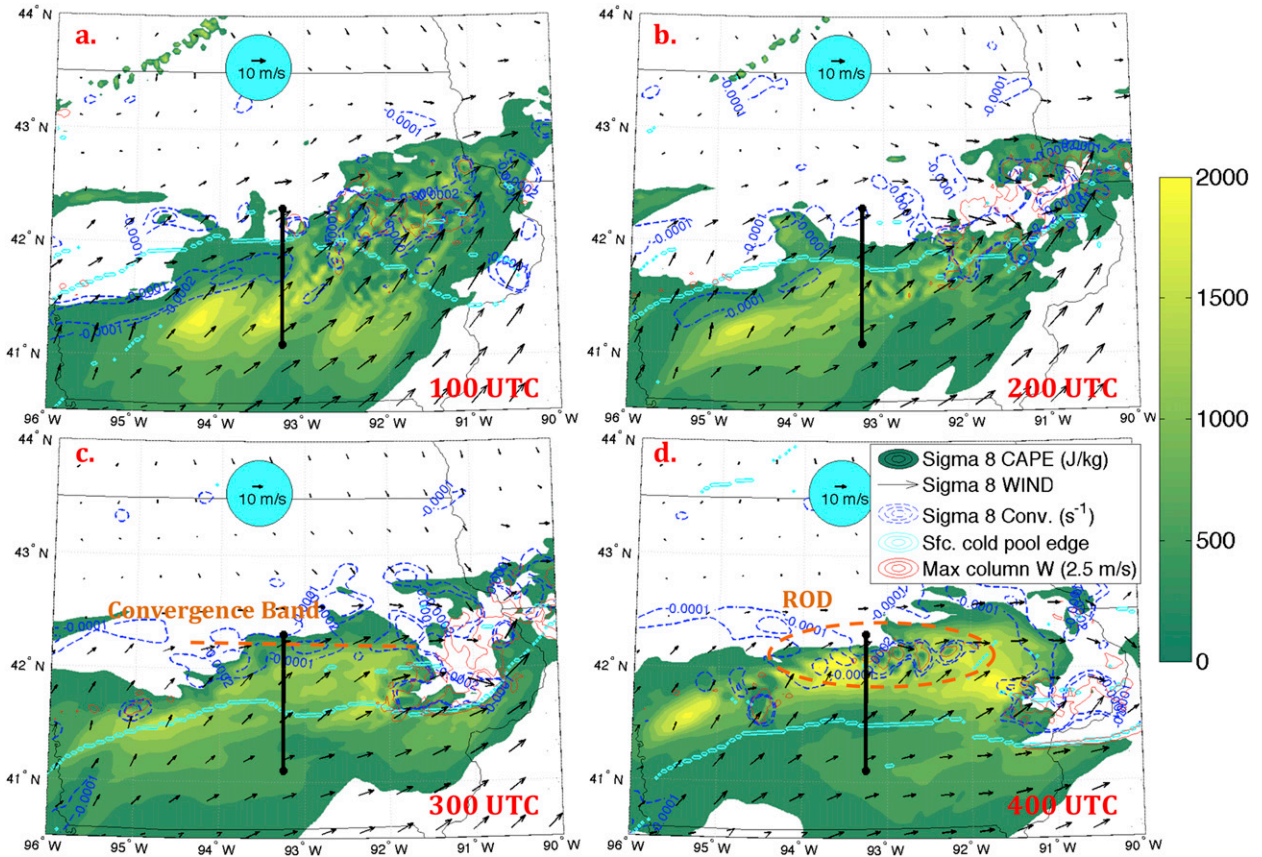
FIG. 13. CAPE for parcels lifted from the eighth model sigma level (shading), flow vectors on the eighth model sigma level (black arrows), convergence on the eighth model sigma level (blue dotted contours, starting at $-1 \times 10^{-4}\,\mathrm{s}^{-1}$ and decreasing at intervals of $-1 \times 10^{-4}\,\mathrm{s}^{-1}$), surface cold pool boundaries defined as a local maxima in the surface temperature gradient in conjunction with a decrease in potential temperature of 2 K or more within eight grid points to the north (cyan lines), and maximum column vertical velocity (red contour corresponding to 2.5 m s^{-1}). Valid times on 28 Jul 2011 are listed in the bottom-right corner. The solid black vertical line indicates the path of cross sections shown in Figs. 14 and 15.

associated with negative ratios is small and shallow, when compared to positive ratios. In cases where convective systems produce radial outflow in a vertically sheared environment, the sense of the $C/\Delta U$ ratio will favor convective development along the downshear outflow boundary (where the vertical wind shear vector points from cold to warm air) as opposed to the upshear outflow boundary (where the vertical wind shear vector points from warm to cold air). The aforementioned principles suggest that the vertically varying shear direction evident in Fig. 4 (as is common for TL/AS-type systems) was likely a contributing factor to the propensity for convection to persist near the southeastern cold pool periphery, while remaining well removed from the southwestern cold pool periphery.

Figure 18 shows vertical wind shear vectors over the depth of the cold pool (ΔU) in the warm air to the south of the cold pool from 0300 (Fig. 18a) to 0600 UTC (Fig. 18d). Estimated cold pool velocity vectors (see

figure caption for the computation of this quantity) are also included to facilitate understanding of the motion (or lack thereof) of the outflow boundary over this time frame. While we do not quantitatively address the $C/\Delta U$ ratio (as in Rotunno et al. 1988), we may consider situations in Fig. 18 along the cold pool edge in which ΔU vectors point toward warm air (cold air) as being the favorable (unfavorable) flanks of the cold pool for sustained triggering of convection.

Favorable wind shear conditions existed for initiating convection along the surging southeastern periphery of the cold pool at 0300 UTC (Fig. 15a), where robust convection resided near the outflow boundary. Along the southwestern cold pool periphery (to the south of the upstream wake region of the progressive MCS segment); however, vertical wind shear over the cold pool depth was minimal during the 0300–0400 UTC time frame (Figs. 15a,b). This resulted in suboptimal lifting along the boundary, which was apparently insufficient to
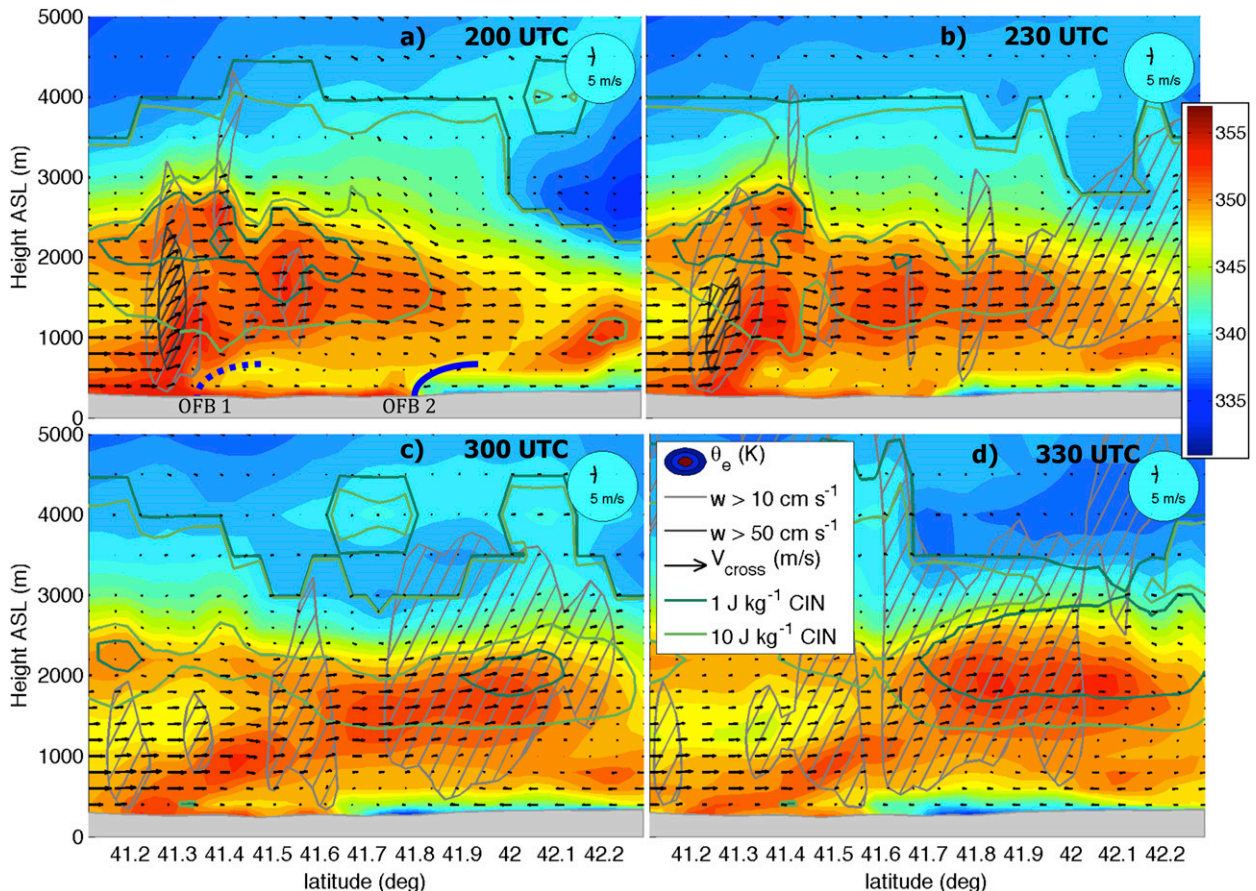
FIG. 14. Cross sections along the black line in Fig. 13 of equivalent potential temperature (θ_e, shading), the 1 and 10 J kg^{-1} convective inhibition contours (CIN, dark and light green solid lines, respectively), cross-sectional parallel wind vectors (black arrows, m s^{-1}), and regions of vertical velocity > 10 cm s^{-1} (hatched light gray regions) and 50 cm s^{-1} (hatched dark gray regions).

overcome the substantial CIN in the lower troposphere evident in Fig. 14. Surface wind vectors within the cold pool near the outflow boundary were oriented nearly parallel to the outflow boundary between 0300 (Fig. 18a) and 0400 UTC (Fig. 18b), which contributed to the nearly stationary character of the boundary over this time frame. In contrast, flow direction within the cold pool along the southeastern periphery was strongly oriented perpendicular to the boundary, which contributed to the substantial southeastward movement of the boundary over the same time frame.

By 0500 UTC (Fig. 15c), ΔU vectors along the far southwestern cold pool periphery were oriented toward the cold pool. Convection along the western MCS flank had generated an enhanced local surface cold anomaly at this time (Fig. 11b), resulting in a new outflow boundary being analyzed just to the south of the convective line (this feature is notated in the 0500 UTC panel in Fig. 9). By 0600 UTC (Fig. 18d), however, the outflow boundary that had been newly analyzed at

0500 UTC (Fig. 18c) had moved southward, while the convective line remained stationary (this event constituted the onset of the second ROD episode). The southward movement of the new outflow boundary between 0500 (Fig. 18c) and 0600 UTC (Fig. 15d) likely resulted from a substantial northerly wind component within the cold pool and orthogonal to the outflow boundary over this time frame. The ΔU vectors along this outflow boundary remained unfavorably oriented toward the cold pool between 0500 (Fig. 15c) and 0600 UTC (Fig. 18d), potentially explaining why convection did not "follow" the outflow boundary southward.

5. Dynamical mechanisms for MCS organization

The low-level flow changes occurred as the eastward-moving convective segments influenced the behavior of the MCSs in several ways. Low-level flow to the rear of convective segments temporarily turned from southwestward to westward, which disrupted the transport of
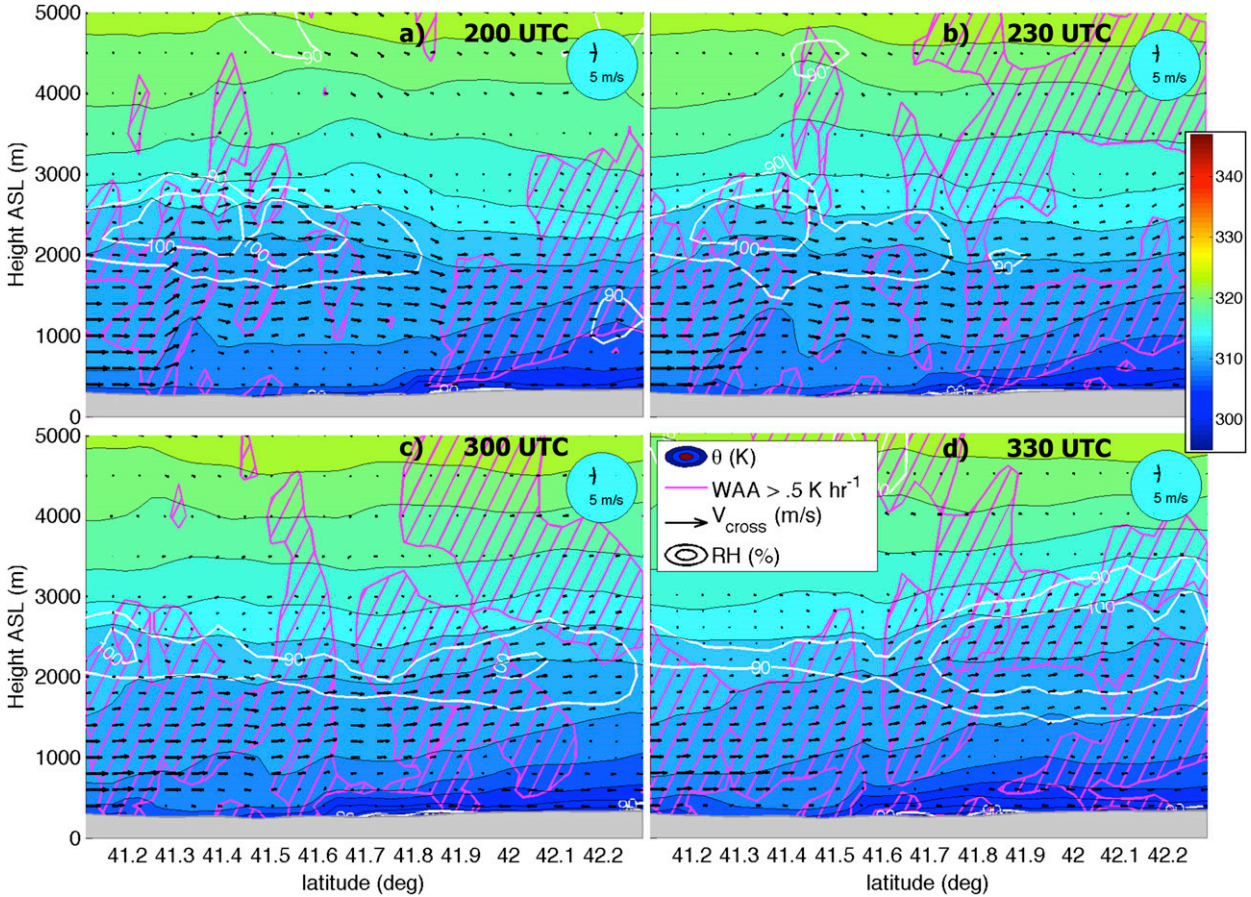
FIG. 15. Cross sections along the black line in Fig. 13 of potential temperature (θ, shading), the 90% and 100% relative humidity contours (white solid lines), cross-sectional parallel wind vectors (black arrows, m s^{-1}; arrows lengths have been scaled so that the ratio of the units of the horizontal and vertical velocity components is unity), and regions of warm air advection > 0.5 K h^{-1} (hatched regions).

potentially unstable air to the region where ROD would eventually occur. The low-level flow direction in the aforementioned region then returned to southwesterly, allowing for potentially unstable flow to travel northward past the surface outflow boundary and eventually trigger ROD convection. In this section we analyze the low-level horizontal momentum budget in order to better understand the mechanisms for this behavior.

a. Analysis framework

Starting with the anelastic horizontal momentum equation in height coordinates (bold letters denote vectors):

$$\frac{\partial \mathbf{V}_h}{\partial t} = -(\mathbf{V} \cdot \nabla)\mathbf{V}_h - \frac{1}{\rho_0}\nabla_h p - f\mathbf{k}\times\mathbf{V}, \qquad (1)$$

where $\mathbf{V}_h$ is the horizontal wind velocity vector and all other terms retain their traditional meanings, we

separated the contributions to the local time tendency into those due to the separate terms on the right-hand side (rhs) of Eq. (1):

$$\left(\frac{\partial \mathbf{V}_h}{\partial t}\right)_{\text{HM}} = -(\mathbf{V}_h \cdot \nabla)\mathbf{V}_h, \qquad (2)$$

$$\left(\frac{\partial \mathbf{V}_h}{\partial t}\right)_{\text{VM}} = -w\frac{\partial \mathbf{V}_h}{\partial z}, \qquad (3)$$

$$\left(\frac{\partial \mathbf{V}_h}{\partial t}\right)_{\text{PG}} = -\frac{1}{\rho_0}\nabla_h p - f\mathbf{k}\times\mathbf{V}. \qquad (4)$$

Here, we have assumed large-scale atmosphere dominated by geostrophic balance, and convectively induced flow deviations from geostrophy, therefore, dominate the rhs of Eq. (4).

To estimate the contributions to the change in wind through a layer in the atmosphere during a specified
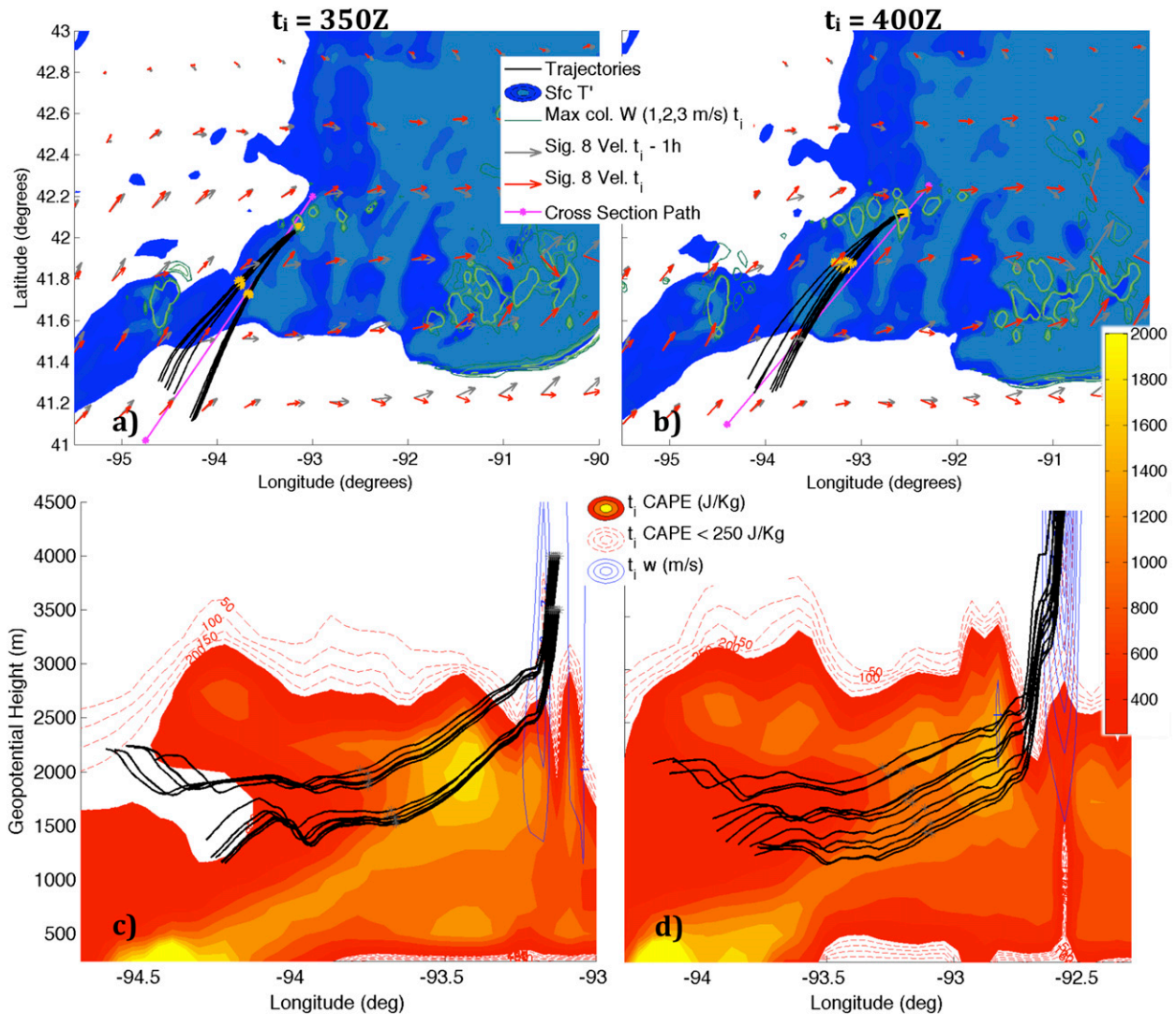
FIG. 16. (a),(b) The horizontal path of back trajectories initialized within updrafts (black lines with yellow markers denote the location at initialization, and 1 h prior to initialization), surface -1-K potential temperature anomalies at the time of trajectory initialization (shading, -2-, -1.5-, -1-, $-0.$-K contours), maximum column vertical velocities at the time of trajectory initialization (solid green contours, 1, 2, and 3 m s^{-1}), and wind vectors at the time of trajectory initialization (red arrows) and 1 h prior to trajectory initialization (green arrows) on the eighth model sigma level. (c),(d) Cross sections of CAPE (shading, J kg^{-1}) and vertical velocities (blue solid contours, m s^{-1}) along the magenta dashed lines with asterisk ends in the top panels valid at the trajectory initialization times. Red dotted contours show CAPE values below the shading threshold of 250 J kg^{-1}. Trajectory paths are projected onto the cross sections (black lines). Trajectory initialization times (t_i) for each column of figure panels are listed above the top panels, and initialization heights were 3500 and 4000 m for the 0350 UTC initializations (as evident in the figure), and 5800 and 6800 m for the 0400 UTC initializations.

period of time, we temporally integrated the rhs of Eqs. (2)–(4). For instance, when these operations are applied to Eq. (4), we obtain the following:

$$
\Delta \mathbf{V}_{\mathrm{PG}}(t_1, t_2, x, y, z)
$$
$$
= - \int_{t_1}^{t_2} \left[\frac{1}{\rho_0(z)} \nabla_h p(t, x, y, z) + f \mathbf{k} \times \mathbf{V}(t, x, y, z) \right] dt,
$$

(5)

where the Δ symbol denotes the local velocity difference between t_2 and t_1. All integrations were estimated by Riemann summations over model output at 10-min intervals. These time-integrated quantities are hereby referred to in the text as $\Delta \mathbf{V}_{\mathrm{HM}}$, $\Delta \mathbf{V}_{\mathrm{VM}}$, and $\Delta \mathbf{V}_{\mathrm{PG}}$, respectively.

b. Spatial patterns of dynamical quantities

We analyzed the quantities $\Delta \mathbf{V}_{\mathrm{HM}}$, $\Delta \mathbf{V}_{\mathrm{VM}}$, and $\Delta \mathbf{V}_{\mathrm{PG}}$ at the 1.5-km level over two separate time periods:
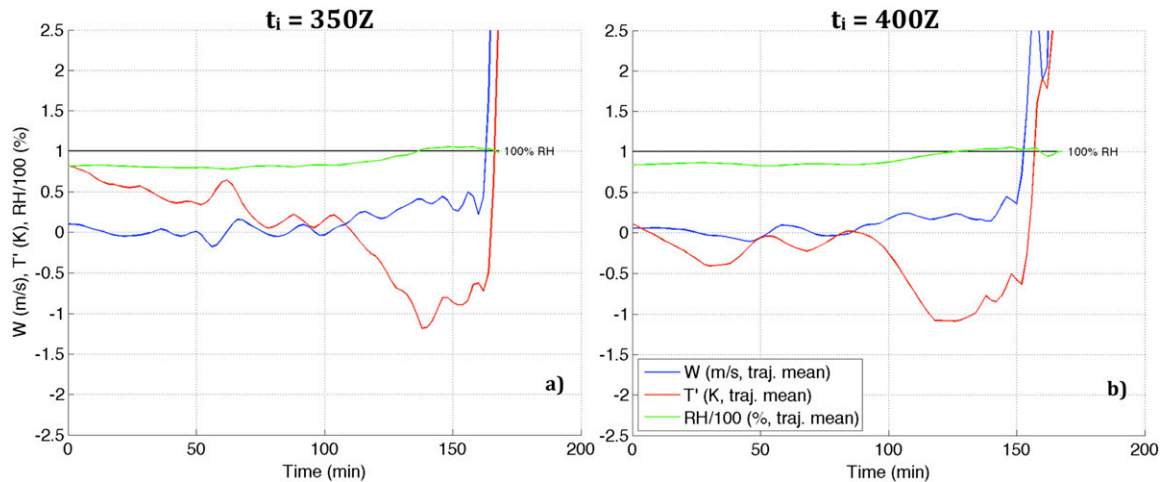
FIG. 17. Time series of mean vertical velocities (blue lines, m s^{-1}), potential temperature anomalies (red lines, K), and relative humidity (green lines, %/100) over all trajectory paths for back trajectories initialized at (a) 0350 and (b) 0400 UTC.

0100–0400 UTC 28 July (Fig. 19) and 0400–1000 UTC 28 July (Fig. 20). The former time frame was chosen in order to investigate mechanisms for changes to the low-level horizontal wind that occurred to the rear of the first progressive convective segment, and to determine how such wind changes may have contributed to the behavior of the MCS. The time frame of the passage of the progressive convective segment through box 1 in Fig. 19 was 0100–0300 UTC (see simulated radar reflectivity in Fig. 10), and ROD occurred in this region began between 0350 and 0400 UTC.

The $\Delta\mathbf{V}_{PG}$ vectors were northerly through the northern portion of box 1 and turned westerly through the central and southern portions of boxes 1 and 2, suggesting that low-level pressure perturbations associated with the passage of the initial progressive MCS were responsible for the changes of the low-level from southwesterly to westerly in this region (this change is evident in Fig. 11a). Low-level temporally averaged low pressure perturbations coincide well with regions of midtropospheric temporally averaged warming in convective updrafts (which is maximized in the region affected by the progressive MCS; Fig. 17d), implicating latent heating in the generation of such low-level pressure anomalies. These patterns are consistent with mechanisms for MCS rear-inflow-jet generation in squall lines (Smull and Houze 1987; Weisman 1992), where buoyancy-induced low-level low pressure perturbations along the progressive convective line promote horizontal flow accelerations into the rear of the line.

The $\Delta\mathbf{V}_{VM}$ vectors were northeasterly in the eastern portion of box 1 (the primary region affected by the passage of the progressive MCS), whereas $\Delta\mathbf{V}_{HM}$

vectors were southwesterly through nearly the same region. We may conjecture here that (i) the former is primarily a result of upward transport resulting from deep convective overturning—that is, flow with southwesterly low-level wind shear encountering regions of upward motion, resulting in the replacement of fast southwesterly wind at this level with slower southwesterly wind from below, and (ii) the latter is primarily a result of unmodified (where "modified" refers to convectively altered) southwesterly flow within the low-level jet replacing modified westerly and northwesterly flow to the rear of the initial progressive MCS (both of these arguments were deduced from the wind structures evident in Figs. 11 and 12). Note that while the latter argument is rather intuitive based on an investigation of Fig. 12a, the former will be investigated more comprehensively in the next section. The patterns of $\Delta\mathbf{V}_{VM}$ and $\Delta\mathbf{V}_{HM}$ were similar during 0400–1000 UTC (Fig. 20) to those evident in Fig. 17, and we may invoke similar arguments to (i) and (ii) earlier in this section to explain their patterns.

The pattern of $\Delta\mathbf{V}_{PG}$ during 0400–1000 UTC (Fig. 20) is notably different than that during 0000–0400 UTC (Fig. 19), exhibiting northeasterly orientation in the western portion of box 1, northwesterly orientation west of box 1, and small magnitude elsewhere. This shows that pressure gradient forces along the line acted to maintain the confluent flow pattern that had initially been generated by the first eastward-moving convective segment. While the low pressure anomaly evident during 0000–0400 UTC was not present during this time frame, a regional low pressure anomaly had developed along the upstream end of the convective line, with the minimum in low-level low pressure (near the west side
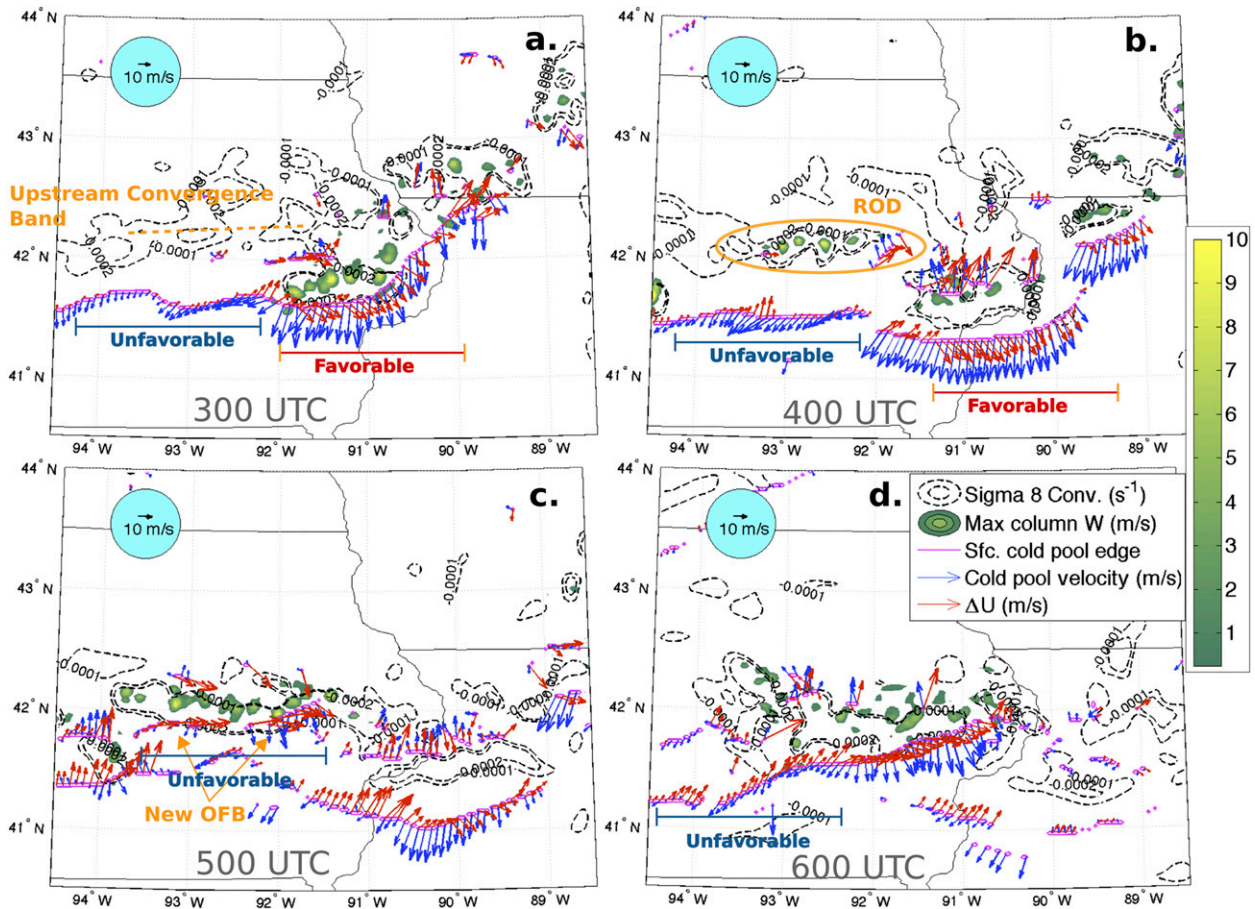
FIG. 18. Maximum column vertical velocity (shading, starting at $1\,\mathrm{m\,s^{-1}}$), convergence on the eighth model sigma level (black dotted contours, starting at $-1\times10^{-4}\,\mathrm{s^{-1}}$ and decreasing at intervals of $-1\times10^{-4}\,\mathrm{s^{-1}}$), surface cold pool boundaries (magenta lines, as defined in the Fig. 13 caption), estimated cold pool velocity vectors along the cold pool boundary (blue arrows), and estimated vertical wind shear vectors over the depth of the cold pool at the cold pool boundary (red arrows). Cold pool velocity vectors were estimated by the wind velocity four grid points north of a given point on the magenta line (within the cold pool), and vertical wind shear vectors ($\Delta\mathbf{U}$) were estimated as the vector difference between the wind four grid points south of a given point on the magenta line at the height of the cold pool depth (defined as the height of the first instance in the vertical of $\theta' > -0.5\,\mathrm{K}$) and the surface wind velocity at that point. Valid times on 28 Jul 2011 are listed at the bottom of each panel.

of box 1) having coincided with a maximum in upper-tropospheric heating. Once again, the coincidence between upper-level heating and low-level low pressure suggests that the former was responsible for, or enhanced the latter.

Figure 21 reveals that the low pressure anomaly west of the MCS extended well beyond the immediate region of convection associated with the convective system, which suggests that large-scale processes were partially responsible for the presence of this feature. A marked deepening of the low close to convection on the western end of the system is evident between 0700 (Fig. 21a) and 0900 UTC (Fig. 21c), further suggesting that convective latent heating enhanced this feature. North–south-oriented cross sections (Fig. 21d) just east of the local maximum low pressure reveal upward-sloping isentropes

with northward extent within southerly flow feeding up-drafts (specifically between 41.7° and 41.9°N in Fig. 21d), along with gradually increasing relative humidity within this flow prior to its entry into updrafts. This in combination with downward-sloping isentropes at midlevels above the region of low-level upslope is similar to the pattern typically observed in association with MCVs (Raymond and Jiang 1990; Schumacher and Johnson 2008, see their Fig. 3). The upstream low pressure anomaly may have facilitated upstream backbuilding by locally enhancing low-level isentropic uplglide (see Figs. 21a–c) and layer lifting, priming air parcels for entry into deep convection.

Two additional sets of back trajectories were initialized at 0650 and 0740 UTC within two separate updrafts along the upstream (western) flank of the MCS where
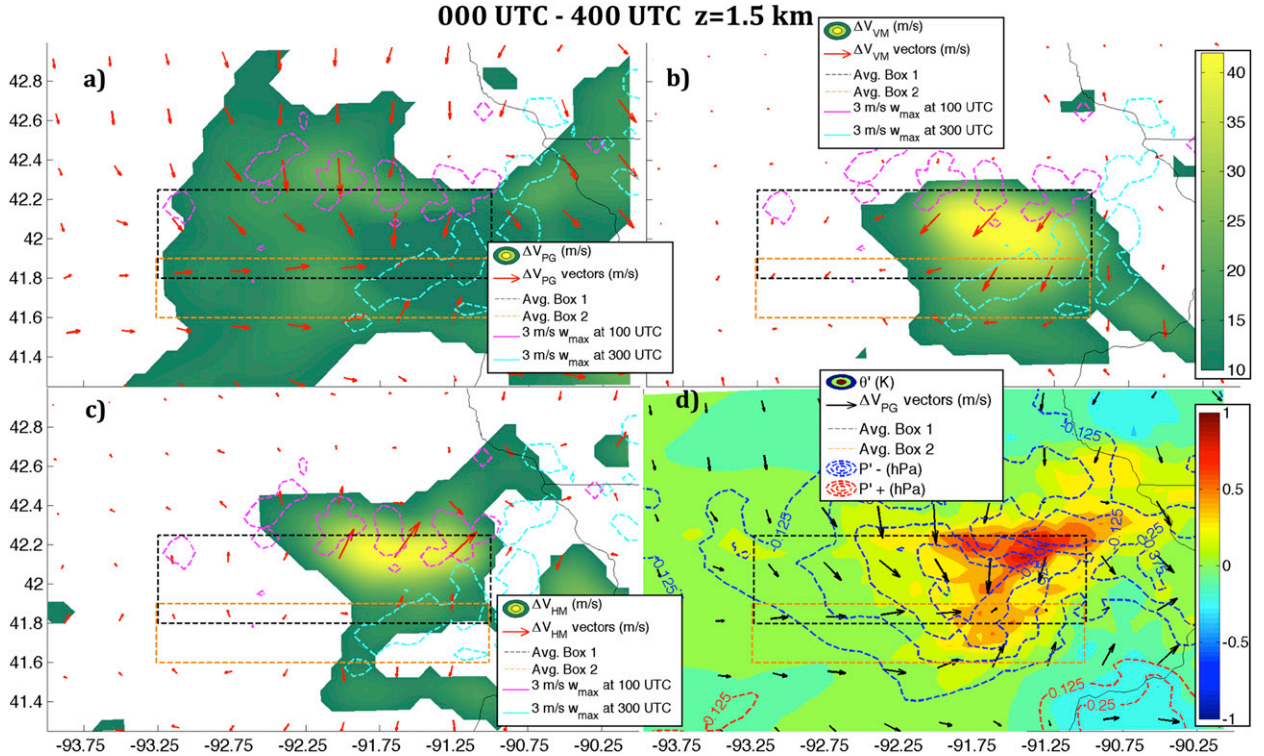
FIG. 19. (a) The magnitude of $\Delta\mathbf{V}_{PG}$ (shading, m s^{-1}) and $\Delta\mathbf{V}_{PG}$ vectors (red arrows). (b) The magnitude of $\Delta\mathbf{V}_{VM}$ (shading, m s^{-1}) and $\Delta\mathbf{V}_{VM}$ vectors (red arrows). (c) The magnitude of $\Delta\mathbf{V}_{HM}$ (shading, m s^{-1}) and $\Delta\mathbf{V}_{HM}$ vectors (red arrows). (d) Temporally averaged 2–10-km potential temperature anomalies (shading, K), temporally averaged pressure anomalies [hPa: negative (blue dashed contours) and positive (red dashed contours)], and $\Delta\mathbf{V}_{PG}$ vectors (black arrows). (a)–(c) The 3 m s^{-1} maximum column vertical velocity contours at 0100 UTC (magenta contour) and 0300 UTC (cyan contour) 28 Jul 2011. In (a)–(d) spatial average boxes for time series computations in Fig. 24. All quantities aside from maximum column vertical velocities and temporally averaged potential temperature anomalies were assessed on the 1.5-km geopotential height surface. Temporal integrations and averages were computed from 0000 to 0400 UTC.

sustained upstream backbuilding was occurring. The horizontal and vertical paths of these trajectories are shown in Fig. 22. Analogous diagnostic quantities to those shown in Fig. 17 are shown for the 0650 and 0740 UTC trajectory initializations in Fig. 23. Air parcels that eventually entered updrafts once again originated well above the surface—between the 2000- and 2500-m geopotential height levels (the surface height here was ~300 m). CAPE values to the rear of the system were far lower than those associated with ROD convection between 0400 and 0500 UTC (Figs. 23c,d, which is consistent with the diminishing CAPE magnitudes after 0400 UTC in this region evident in Fig. 14), and in some cases their origins appear to be above the level of maximized CAPE (Figs. 23c,d, this is especially evident in the analysis of the trajectories initialized at 0650 UTC). There are also indications of 30–60 min of gradual layer lifting within the paths of the air parcels (Fig. 24), similar to those evident in the analysis of the previous two back-trajectory analyses (e.g., steady gradual vertical motion, decreasing T' values, and increasing RH prior to the entry of parcels into a convective updraft).

c. Influence of dynamical quantities on the MCS evolution

The magnitude of the southerly component of southwesterly inflow into the western end of the MCS briefly abated during both southward cold pool surge events, which disrupted the supply of high CAPE air to the upstream end of the MCS, and resulted in a temporary cessation of the training of convection (as illustrated in section 4a). In this subsection, we analyze the time series (Fig. 24) of the instantaneous local tendencies [e.g., Eqs. (2)–(4)], along with the time-integrated changes in the v-wind component [e.g., Eq. (5)] to better understand the mechanisms for these cold pool surges. Since the mean tropospheric flow (see the 1–10-km mean wind in Figs. 24b,d,f,h) was oriented northward throughout the lifetime of the MCS, southward
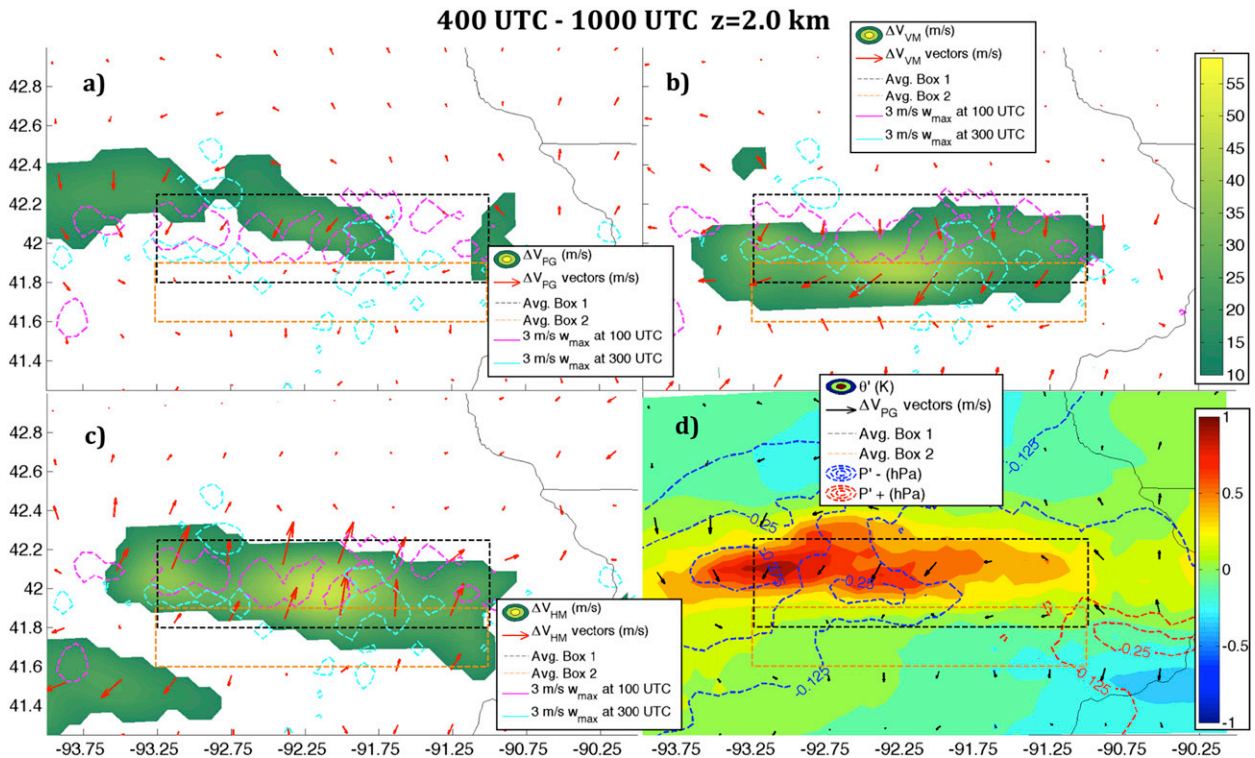
FIG. 20. (a)–(d) As in Fig. 19, but for 0400–1000 UTC and on the 2.0-km geopotential height surface. The $3 \, \text{m s}^{-1}$ maximum column vertical velocity contours now correspond to 0500 (magenta) and 0700 UTC (cyan).

movement of convection during cold pool surges was likely related to propagation along the cold pool edge rather than fluctuations in the orientation of steering flow.

We focused on the dynamics of the two southward cold pool surges that preceded ROD episodes considering: accelerations in the 0–1-km geopotential height layer (hereby "lower layer;" the approximate depth of the cold pool); and on the accompanying changes to the low-level flow structure (low level refers to flow just above the cold pool in the maximum CAPE layer) by considering analogous accelerations in the 1–2-km (0000–0400 UTC) and 1.5–2.5-km (0400–1000 UTC) layers (hereby "upper layer;" the approximate low-level inflow and maximum potential instability layer). The upper layer was raised 0.5 km for the second time frame to avoid the influence of the cold pool (which had deepened by this time frame).

The terms $(\partial v/\partial t)_{PG}$ and $(\partial v/\partial t)_{VM}$ (hereafter denoted δPG and δVM, respectively) exhibited southerly tendencies that peaked during the first cold pool surge (~0150–0300 UTC; Figs. 19a,c), while $(\partial v/\partial t)_{HM}$ (δHM) exhibited an opposing northerly tendency. Furthermore, because the vertical velocity (and thus the momentum transport) was primarily upward during this time period,

this corroborates our earlier conjecture that upward transport of southerly momentum away from this layer (especially along the outflow boundary where low-level upward motion is common) was the primary process related to δVM at work here. The mechanism for a surging cold pool in the lower layer likely resulted from pressure gradient accelerations driven by the cold pool mesohigh (see Fig. 20) and vertical motion along the cold pool edge (and thus upward momentum transport) having been sufficiently strong to overcome opposing ambient southerly flow. These factors resulted in a change from $5 \, \text{m s}^{-1}$ southerly flow at 0000 UTC to nearly $5 \, \text{m s}^{-1}$ northerly flow at 0250 UTC (Fig. 19b) in the lower layer. Similar tendency patterns were evident in the upper layer, as southward δPH and δVM reduced the initial $10 \, \text{m s}^{-1}$ southerly flow in this layer to near zero during the first cold pool surge by 0230 UTC (Fig. 19d). This was followed by a strong southerly wind tendency contributed by δHM at ~0230–0240 UTC (Fig. 19c; this is likely the low-level flow "resurgence" described in section 4b, see Fig. 20) resulting in an increase in the southerly flow magnitude to 1–$2 \, \text{m s}^{-1}$.

During the second cold pool surge (which occurred between 0500 and 0600 UTC), δPG and δVM once again
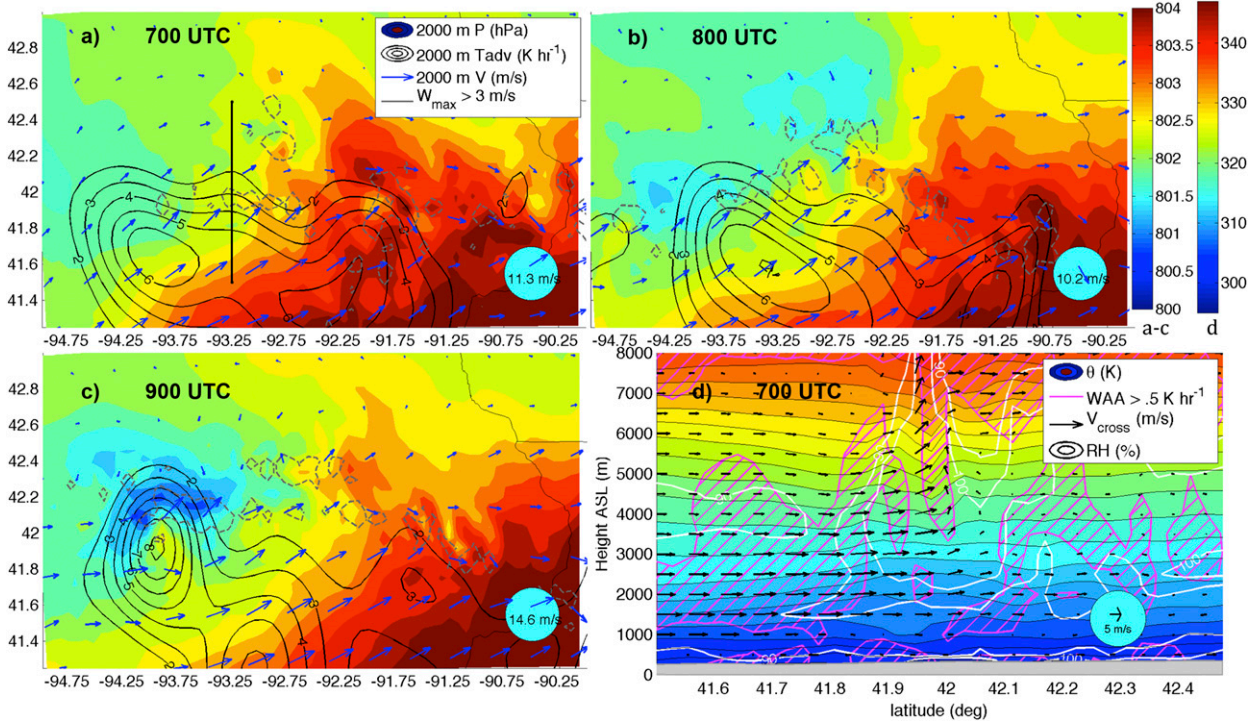
FIG. 21. (a)–(c) Pressure on the 2-km geopotential height surface [shading, hPa, see left color bar to right of (b)], 2-km horizontal warm air advection (black contours, K h^{-1}), 2-km horizontal wind vectors (blue arrows, m s^{-1}), and the 3 m s^{-1} maximum column vertical velocity contour (black dashed). (d) As in Fig. 15, but at 0700 UTC along the black solid line in (a) (see right color bar).

exhibited southerly tendencies in the lower layer in box 2 (Fig. 19e). Box 2 was chosen for the lower-layer analysis during this time frame in order to adequately capture southward accelerations associated with the cold pool—the signatures of such accelerations were less apparent in box 1. Note that δHM was initially oriented northward at 0500 UTC, but shifted to a southward orientation by 0600 UTC. This is likely a result of northerly flow within the cold pool inundating this region as the outflow boundary moved south of the southern boundary of the box, combined with a northward-oriented gradient in the magnitude of v. The aforementioned southward accelerations contributed to a brief southerly wind of 5 m s^{-1} between ~530 and 0700 UTC (the outflow boundary passage) within this layer (Fig. 19f).

The terms δPG and δVM contributed predominantly southward tendencies in the upper layer between 0400 and 1000 UTC (Fig. 19g), with the exception of brief northward δPG orientation before and during the second cold pool surge at 0430 and 0530 UTC. The behavior of δPG is consistent with low-level northerly accelerations into updrafts. The magnitude of southward δVM was maximized during the development of ROD convection [~(0400–0500 UTC)] and the second cold pool surge [~(0500–0630 UTC)]. Upward momentum

transport was once again the predominant contributor to δVM during the cold pool surge, pointing to upward transport of southwesterly momentum away from this layer as the primary process here. After 0630 UTC, the contribution from downward momentum transport exceeded that of upward momentum transport, suggesting that downward transport of northerly momentum played a significant role beyond that time. The δHM exhibited a consistent northward tendency throughout the 0400–1000 UTC time frame, which likely reflects a persistent northward push of southerly momentum within the low-level jet. The magnitude of the net wind tendency gradually decreased toward the end of the time frame as the aforementioned forces approximately balanced each other.

In summary, cold pool surges occurred when the cold pool became sufficiently strong to induce a southward-oriented pressure gradient, lifting along the cold pool edge transported southerly flow south of the cold pool above it, and southward tendency due to these factors became sufficiently strong to overcome the northward push ("push" refers to the role of δHM) of unmodified near-surface flow.

As discussed earlier, convection propagated along the southeastern cold pool flank during each southward cold pool surge. As convection moved south,
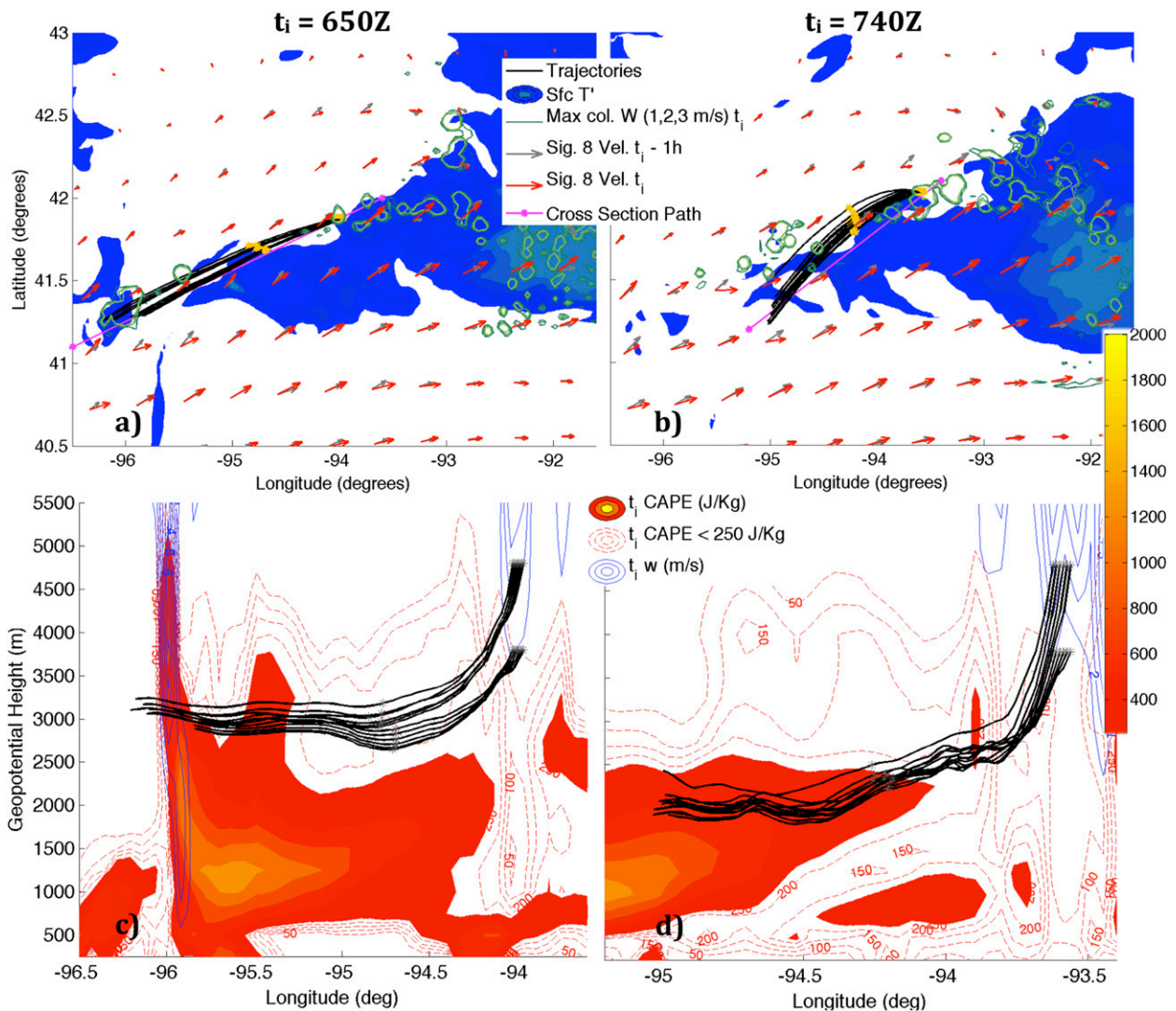
FIG. 22. As in Fig. 16, but for back trajectories initialized at the listed times. Initialization heights were 3800 and 4800 m for both initialization times (as evident in the figures).

upward momentum transport of southerly flow in convective updrafts away from the layer of instability, downward transport of northerly momentum into this layer in convective downdrafts, and southward pressure gradient accelerations into the rear of convective updrafts (relative to their motion) combined to exhibit a southward wind tendency. This southward tendency canceled the southerly component of southwesterly MCS-relative inflow, interrupting the supply of convective instability to the western end of the CMS and temporarily disrupting upstream backbuilding. Southwesterly inflow then reentered the western flank of the MCS via horizontal momentum advection. These factors—the interruption and subsequent reintroduction of southwesterly MCS-relative inflow, and the fact that

the reintroduced southwesterly flow was sufficiently convectively inhibited (and insufficiently lifted along the boundary) so as to require northward travel beyond the southwestern outflow boundary before gradual lifting could reinitiate convection (as discussed in section 4a)—potentially explain the northward separation of convection from the surface outflow boundary (which is a characteristic of the ROD phenomena).

6. Summary and conclusions

This study details the results and analysis of a numerical simulation of a quasi-stationary MCS that produced a swath of 12-h rainfall in excess of 300 mm across eastern Iowa on 28 July 2011, with the purpose of
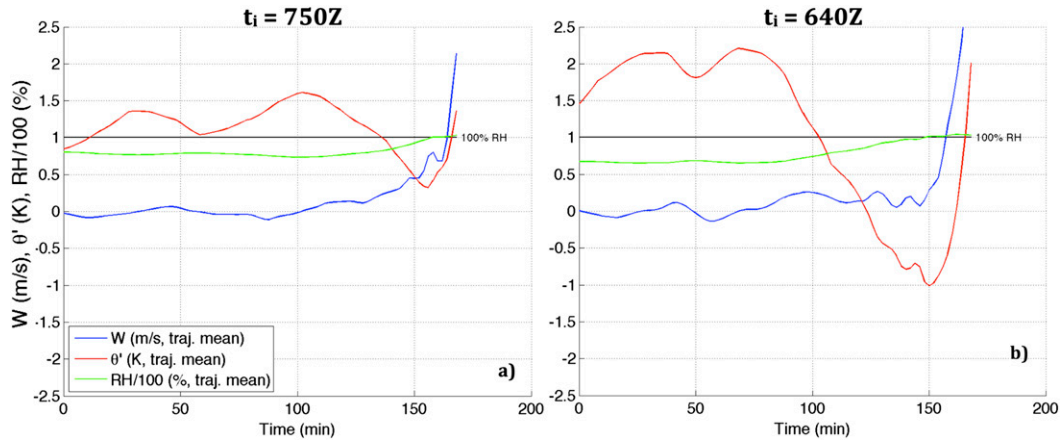
FIG. 23. As in Fig. 17, but for the back trajectory initialization times listed.

elucidating the organizational dynamics of this system. The synoptic-scale environment associated with this system was characteristic of existing synoptic archetypes for warm-season flash-flooding events, and featured a southwesterly low-level jet (which supplied warm, moist air at low levels), persistent low-level convergence and warm air advection, and a quasi-stationary low-level frontal boundary. Our simulation reproduced the salient radar-observed and accumulated rainfall characteristics of the observed MCS. The following summarizes the results from our dynamical analysis of the simulated MCS (A visual summary is depicted in the schematic shown in Fig. 25):

- Despite the presence of a stable boundary layer and elevated maximum CAPE throughout the lifetime of the MCS, a surface cold pool was present throughout the lifetime of the MCS.
- Two southeastward surges of the cold pool and convection occurred in the simulation (one occurred in the observed system). Elevated high θ_e air was transported to the rear of each of these convective segments as they moved out of the region of where the heaviest rainfall occurred. This air was lifted to saturation; CIN was eroded, and the flow triggered new convection [referred to as rearward off-boundary development (ROD)], which reinvigorated heavy rainfall production over the fixed geographic region. Lifting was accomplished by persistent large-scale warm air advection, with potential enhancement from gradual ascent over the cold pool left by earlier convection and an upstream low-level mesolow. Large-scale processes were presumed to have been the impetus for this pressure feature, which was enhanced by latent heating associated with convective updrafts.
- The cold pool–normal vertical wind shear profile over the depth of the cold pool along the southeastern cold

pool flank was more favorable for kinematic lifting along the boundary than the analogous profile along the southwestern cold pool flank. This potentially explains why convection propagated along (did not propagate along) the southeast (southwest) outflow boundary during the lifetime of the MCS. The northward separation of convection from the outflow boundary on the western side of MCS resulted from parcels being convectively inhibited, and insufficiently lifted along the boundary; therefore, requiring additional northward travel and lift to achieve sufficiently expansive saturation and erosion of convective inhibition.
- Cold pool surges that preceded the ROD phenomena occurred when the pressure gradient associated with the cold pool mesohigh and lifting along the outflow boundary (specifically the southeast flank) of southerly flow away from the boundary layer contributed to a net southward flow acceleration along the outflow boundary.
- As convection followed the southeastern cold pool flank during cold pool surges, forces associated with convective overturning changed the wind direction in their wake from southwesterly (providing storm relative inflow of unstable air) to westerly and northwesterly, which temporarily disrupted the supply of instability to the western flank of the MCS. Southwesterly flow associated with the low-level jet then replaced convectively overturned air and reintroduced instability to the western MCS flank, allowing for ROD. These processes explain why upstream back-building was interrupted prior to ROD episodes.

As mentioned earlier in the text, a major caveat to the case-study approach that has been utilized here is that
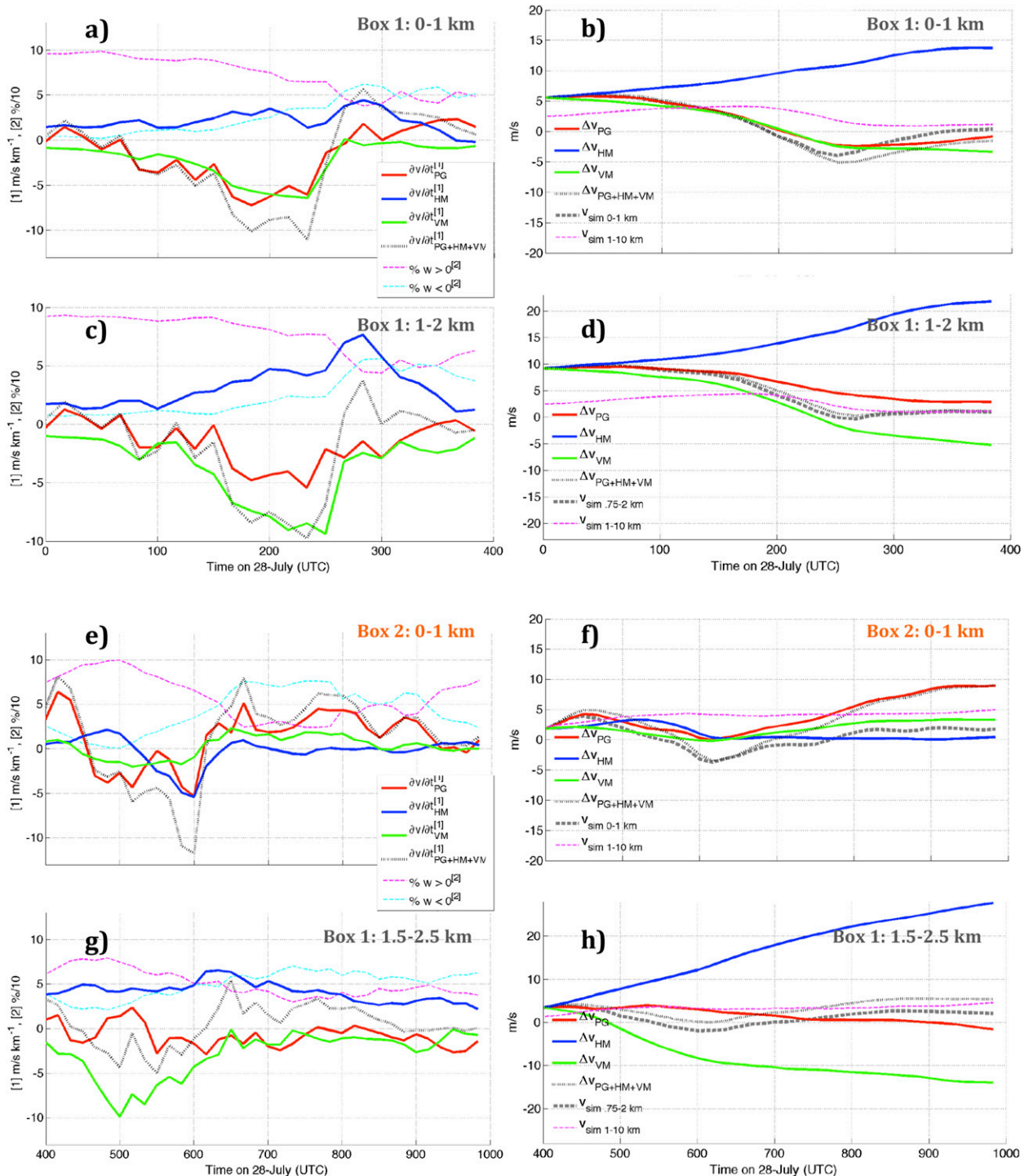
FIG. 24. (a),(c),(e),(g) Time series of the contributions to $\partial v/\partial t$ (m s^{-1} h^{-1}) by pressure gradient accelerations (red lines), horizontal momentum advection (blue lines), vertical momentum advection (green lines), the sum of these contributions (gray dotted lines), the percentage (% $\times 10^{-1}$) of positive contribution to southward vertical momentum advection accelerations by upward momentum advection (magenta dashed lines), and downward momentum advection (cyan dashed lines). (b),(d),(f),(h) Time series of the contributions to $\Delta v + v_i$ by pressure gradient accelerations (red lines, m s^{-1}), horizontal momentum advection (blue lines, m s^{-1}), vertical momentum advection (green lines, m s^{-1}), the sum of these contributions (gray dotted lines, m s^{-1}), the simulated v-wind component (black dashed lines), and the pressure-weighted mean 1–10-km v-wind component (magenta dashed lines; v_i, the v component of the wind at the beginning of each time series, has been added to each quantity in these panels). Times in (a)–(d) are from 0000 to 0400 UTC 28 Jul 2011 and times in (e)–(h) are from 0400 to 1000 UTC 28 Jul 2011. Computations aside from 1–10-km mean winds were averaged horizontally over (a)–(d),(g),(h) box 1 and (e),(f) box 2 and vertically over (a),(b),(e),(f) the 0–1-km layer; (c),(d) the 1–2-km layer; and (g),(h) the 1.5–2.5-km layer.
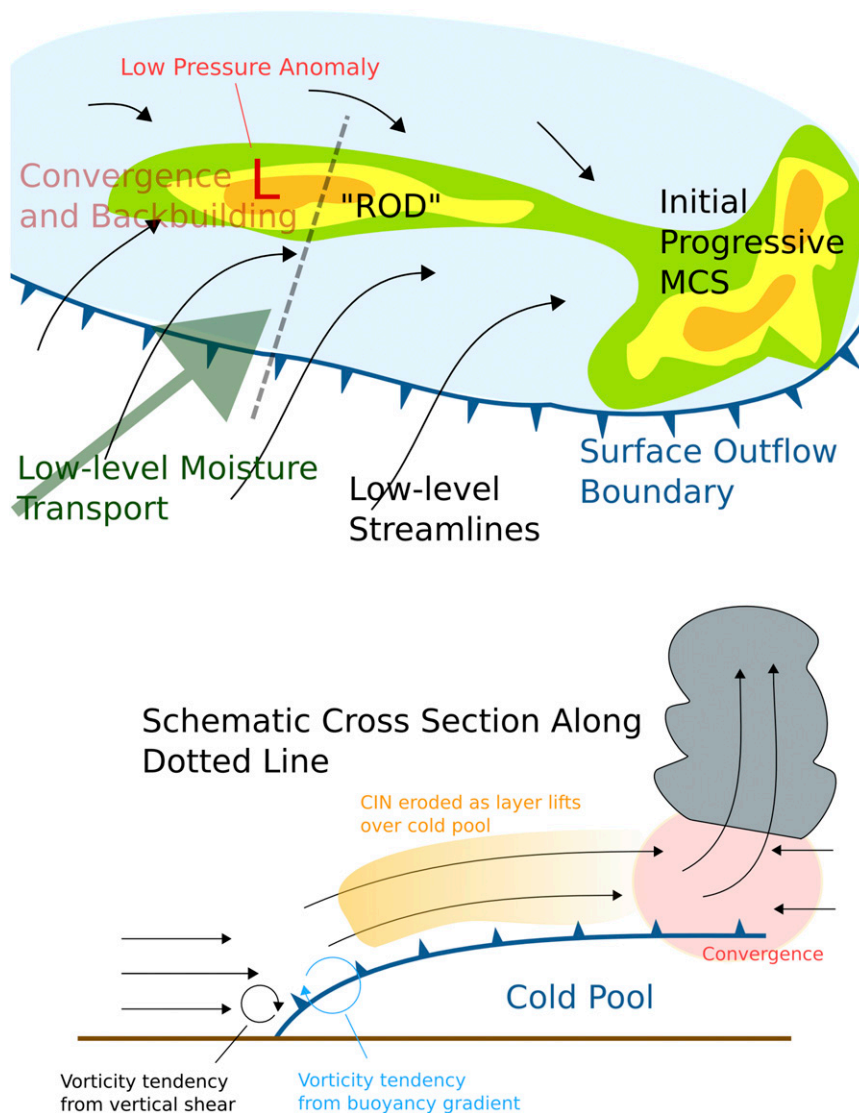
FIG. 25. Schematic diagram of the salient features and processes associated with the 28 Jul 2011 TL/AS MCS.

there is no guarantee that the dynamical insight obtained from such studies may be applied in a general sense to all cases that exhibit a particular convective morphology. Additionally, many of the dynamical fields that were analyzed here exhibited considerable ''noise'' due to prior and concurrent episodes of convection adjacent to the convective system that was analyzed. Future articles aim to develop a more generalized picture of the overall dynamics governing the MCS behaviors detailed in this study through the use of idealized modeling frameworks.

REFERENCES

Augustine, J. A., and F. Caracena, 1994: Lower-tropospheric precursors to nocturnal MCS development over the central United States. *Wea. Forecasting,* **9,** 116–135, doi:10.1175/1520-0434(1994)009<0116:LTPTNM>2.0.CO;2.

Barnes, S., 1964: A technique for maximizing details in numerical weather map analysis. *J. Appl. Meteor.,* **3,** 396–409, doi:10.1175/1520-0450(1964)003<0396:ATFMDI>2.0.CO;2.

Benjamin, S. G., G. A. Grell, J. M. Brown, T. G. Smirnova, and R. Bleck, 2004: Mesoscale weather prediction with the RUC hybrid isentropic–terrain-following coordinate model. *Mon. Wea. Rev.,* **132,** 473–494, doi:10.1175/1520-0493(2004)132<0473: MWPWTR>2.0.CO;2.

Bosart, L. F., and F. Sanders, 1981: The Johnstown Flood of July, 1977: A long-lived convective system. *J. Atmos. Sci.,* **38,** 1616–1642, doi:10.1175/1520-0469(1981)038<1616:TJFOJA>2.0.CO;2.

Bryan, G. H., J. C. Wyngaard, and M. Fritsch, 2003: Resolution requirements for the simulation of deep moist convection. *Mon. Wea. Rev.,* **131,** 2394–2416, doi:10.1175/1520-0493(2003)131<2394:RRFTSO>2.0.CO;2.

Chappell, C. F., 1986: Quasi-stationary convective events. *Mesoscale Meteorology and Forecasting,* P. S. Ray, Ed., Amer. Meteor. Soc., 289–310.

Corfidi, S. F., 2003: Cold pools and MCS propagation: Forecasting the motion of downwind-developing MCSs. *Wea. Forecasting,* **18,** 997–1017, doi:10.1175/1520-0434(2003)018<0997: CPAMPF>2.0.CO;2.

——, J. H. Merritt, and J. M. Fritsch, 1996: Predicting the movement of mesoscale convective complexes. *Wea. Forecasting,* **11,** 41–46, doi:10.1175/1520-0434(1996)011<0041: PTMOMC>2.0.CO;2.

——, S. J. Corfidi, and D. M. Schultz, 2008: Elevated convection and castellanus: Ambiguities, significance, and questions. *Wea. Forecasting,* **23,** 1280–1303, doi:10.1175/2008WAF2222118.1.

Crook, N. A., and M. W. Moncrieff, 1988: The effect of large-scale convergence on the generation and maintenance of deep moist convection. *J. Atmos. Sci.,* **45,** 3606–3624, doi:10.1175/1520-0469(1988)045<3606:TEOLSC>2.0.CO;2.

Dee, D. P., and Coauthors, 2011: The ERA-Interim reanalysis: Configuration and performance of the data assimilation system. *Quart. J. Roy. Meteor. Soc.,* **137,** 553–597, doi:10.1002/qj.828.

Doswell, C. A., H. E. Brooks, and R. A. Maddox, 1996: Flash flood forecasting: An ingredients-based methodology. *Wea. Forecasting,* **11,** 560–581, doi:10.1175/1520-0434(1996)011<0560: FFFAIB>2.0.CO;2.

Dudhia, J., 1989: Numerical study of convection observed during the Winter Monsoon Experiment using a mesoscale two-dimensional model. *J. Atmos. Sci.,* **46,** 3077–3107, doi:10.1175/1520-0469(1989)046<3077:NSOCOD>2.0.CO;2.

French, A. J., and M. D. Parker, 2010: The response of simulated nocturnal convective systems to a developing low-level jet. *J. Atmos. Sci.,* **67,** 3384–3408, doi:10.1175/2010JAS3329.1.

Fritsch, J. M., J. D. Murphy, and J. S. Kain, 1994: Warm-core vortex amplification over land. *J. Atmos. Sci.,* **51,** 1780–1807, doi:10.1175/1520-0469(1994)051<1780:WCVAOL>2.0.CO;2.

Grell, G. A., and D. Dévényi, 2002: A generalized approach to parameterizing convection combining ensemble and data assimilation techniques. *Geophys. Res. Lett.,* **29,** doi:10.1029/2002GL015311.

Janjić, Z. I., 1994: The step-mountain eta coordinate model: Further developments of the convection, viscous sublayer, and turbulence closure schemes. *Mon. Wea. Rev.,* **122,** 927–945, doi:10.1175/1520-0493(1994)122<0927:TSMECM>2.0.CO;2.

Johns, R. H., and C. A. Doswell III, 1992: Severe local storms forecasting. *Wea. Forecasting,* **7,** 588–612, doi:10.1175/1520-0434(1992)007<0588:SLSF>2.0.CO;2.

Keene, K. M., and R. S. Schumacher, 2013: The bow and arrow mesoscale convective structure. *Mon. Wea. Rev.,* **141,** 1648–1672, doi:10.1175/MWR-D-12-00172.1.

Kessler, E., 1969: *On the Distribution and Continuity of Water Substance in Atmospheric Circulation. Meteor. Monogr.,* No. 32, Amer. Meteor. Soc., 84 pp.

Klemp, J. B., W. C. Skamarock, and J. Dudhia, 2007: Conservative split-explicit time integration methods for the compressible nonhydrostatic equations. *Mon. Wea. Rev.,* **135,** 2897–2913, doi:10.1175/MWR3440.1.

Laing, A. G., and J. M. Fritsch, 2000: The large-scale environments of the global populations of mesoscale convective complexes. *Mon. Wea. Rev.,* **128,** 2756–2776, doi:10.1175/1520-0493(2000)128<2756:TLSEOT>2.0.CO;2.

Maddox, R. A., C. F. Chappell, and L. R. Hoxit, 1979: Synoptic and mesoscale aspects of flash flood events. *Bull. Amer. Meteor. Soc.,* **60,** 115–123, doi:10.1175/1520-0477-60.2.115.

Mesinger, F., and Coauthors, 2006: North American Regional Reanalysis. *Bull. Amer. Meteor. Soc.,* **87,** 343–360, doi:10.1175/BAMS-87-3-343.

Mitchell, K. E., and Coauthors, 2004: The multi-institution North American Land Data Assimilation System (NLDAS): Utilizing multiple GCIP products and partners in a continental distributed hydrological modeling system. *J. Geophys. Res.,* **109,** D07S90, doi:10.1029/2003JD003823.

Mlawer, E. J., S. J. Taubman, P. D. Brown, M. J. Iacono, and S. A. Clough, 1997: Radiative transfer for inhomogeneous atmosphere: RRTM, a validated correlated-k model for the longwave. *J. Geophys. Res.,* **102,** 16 663–16 682, doi:10.1029/97JD00237.

Moore, J. T., F. H. Glass, C. E. Graves, S. M. Rochette, and M. J. Singer, 2003: The environment of warm-season elevated thunderstorms associated with heavy rainfall over the central United States. *Wea. Forecasting,* **18,** 861–878, doi:10.1175/1520-0434(2003)018<0861:TEOWET>2.0.CO;2.

Morrison, H., and W. W. Grabowski, 2008: A novel approach for representing ice microphysics in models: Description and tests using a kinematic framework. *J. Atmos. Sci.,* **65,** 1528–1548, doi:10.1175/2007JAS2491.1.

National Weather Service Quad Cities Office, cited 2014: Historic heavy rain and flash flooding in Dubuque and Jo Daviess counties07/27–07/28/2011. [Available online at http://www.crh.noaa.gov/dvn/?n=event_072711_dubuqueflashflood.]

Parker, M. D., 2007: Simulated convective lines with parallel stratiform precipitation. Part I: An archetype for convection in along-line shear. *J. Atmos. Sci.,* **64,** 267–288, doi:10.1175/JAS3853.1.

——, 2008: Response of simulated squall lines to low-level cooling. *J. Atmos. Sci.,* **65,** 1323–1341, doi:10.1175/2007JAS2507.1.

——, and R. H. Johnson, 2000: Organizational modes of midlatitude mesoscale convective systems. *Mon. Wea. Rev.,* **128,** 3413–3436, doi:10.1175/1520-0493(2001)129<3413:OMOMMC>2.0.CO;2.

Peters, J. M., and P. J. Roebber, 2014: Synoptic control of heavy-rain-producing convective training episodes. *Mon. Wea. Rev.,* **142,** 2464–2482, doi:10.1175/MWR-D-13-00263.1.

——, and R. S. Schumacher, 2014: Objective categorization of heavy-rain-producing MCS synoptic types by rotated principal component analysis. *Mon. Wea. Rev.,* **142,** 1716–1737, doi:10.1175/MWR-D-13-00295.1.

Raymond, D. J., and H. Jiang, 1990: A theory for long-lived mesoscale convective systems. *J. Atmos. Sci.,* **47,** 3067–3077, doi:10.1175/1520-0469(1990)047<3067:ATFLLM>2.0.CO;2.

Rotunno, R., J. B. Klemp, and M. L. Weisman, 1988: A theory for strong long-lived squall lines. *J. Atmos. Sci.,* **45,** 463–485, doi:10.1175/1520-0469(1988)045<0463:ATFSLL>2.0.CO;2.

Schmidt, J. M., and W. R. Cotton, 1990: Interactions between upper and lower tropospheric gravity waves on squall line structure

and maintenance. *J. Atmos. Sci.,* **47,** 1205–1222, doi:10.1175/1520-0469(1990)047<1205:IBUALT>2.0.CO;2.

Schumacher, R. S., 2009: Mechanisms for quasi-stationary behavior in simulated heavy-rain-producing convective systems. *J. Atmos. Sci.,* **66,** 1543–1568, doi:10.1175/2008JAS2856.1.

——, and R. H. Johnson, 2005: Organization and environmental properties of extreme-rain-producing mesoscale convective systems. *Mon. Wea. Rev.,* **133,** 961–976, doi:10.1175/MWR2899.1.

——, and ——, 2006: Characteristics of U.S. extreme rain events during 1999–2003. *Wea. Forecasting,* **21,** 69–85, doi:10.1175/WAF900.1.

——, and ——, 2008: Mesoscale processes contributing to extreme rainfall in a midlatitude warm-season flash flood. *Mon. Wea. Rev.,* **136,** 3964–3986, doi:10.1175/2008MWR2471.1.

——, and ——, 2009: Quasi-stationary, extreme-rain-producing convective systems associated with midlevel cyclonic circulations. *Wea. Forecasting,* **24,** 555–575, doi:10.1175/2008WAF2222173.1.

Schwartz, C. S., and Coauthors, 2009: Next-day convection-allowing WRF Model guidance: A second look at 2-km versus 4-km grid spacing. *Mon. Wea. Rev.,* **137,** 3351–3372, doi:10.1175/2009MWR2924.1.

Skamarock, W. C., and Coauthors, 2008: A description of the Advanced Research WRF version 3. NCAR Tech. Note NCAR/TN-475+STR, 113 pp. [Available online at http://www.mmm.ucar.edu/wrf/users/docs/arw_v3_bw.pdf.]

Smull, B. F., and R. A. Houze Jr., 1987: Rear inflow in squall lines with trailing stratiform precipitation. *Mon. Wea. Rev.,* **115,** 2869–2889, doi:10.1175/1520-0493(1987)115<2869:RIISLW>2.0.CO;2.

Stensrud, D. J., and J. M. Fritsch, 1993: Mesoscale convective systems in weakly forced large-scale environments. Part I: Observations. *Mon. Wea. Rev.,* **121,** 3326–3344, doi:10.1175/1520-0493(1993)121<3326:MCSIWF>2.0.CO;2.

Thompson, G., R. P. Field, R. M. Rasmussen, and W. D. Hall, 2008: Explicit forecasts of winter precipitation using an improved bulk microphysics scheme. Part II: Implementation of a new snow parameterization. *Mon. Wea. Rev.,* **136,** 5095–5115, doi:10.1175/2008MWR2387.1.

Trier, S. B., and C. A. Davis, 2002: Influence of balanced motions on heavy precipitation within a long-lived convectively generated vortex. *Mon. Wea. Rev.,* **130,** 877–899, doi:10.1175/1520-0493(2002)130<0877:IOBMOH>2.0.CO;2.

——, ——, and D. A. Ahijevych, 2010: Environmental controls on the simulated diurnal cycle of warm-season precipitation in the continental United States. *J. Atmos. Sci.,* **67,** 1066–1090, doi:10.1175/2009JAS3247.1.

——, J. H. Marsham, C. A. Davis, and D. Ahijevych, 2011: Numerical simulations of the post-sunrise reorganization of a nocturnal mesoscale convective system during 13 June IHOP_2002. *J. Atmos. Sci.,* **68,** 2988–3011, doi:10.1175/JAS-D-11-0112.1.

——, C. A. Davis, D. A. Ahijevych, and K. W. Manning, 2014: Use of the parcel buoyancy minimum (Bmin) to diagnose simulated thermodynamic destabilization. Part II: Composite analysis of mature MCS environments. *Mon. Wea. Rev.,* **142,** 967–990, doi:10.1175/MWR-D-13-00273.1.

Weisman, M. L., 1992: The role of convectively generated rear-inflow jets in the evolution of long-lived mesoconvective systems. *J. Atmos. Sci.,* **49,** 1826–1847, doi:10.1175/1520-0469(1992)049<1826:TROCGR>2.0.CO;2.

——, and R. Rotunno, 2004: "A theory for strong long-lived squall lines" revisited. *J. Atmos. Sci.,* **61,** 361–382, doi:10.1175/1520-0469(2004)061<0361:ATFSLS>2.0.CO;2.

——, W. C. Skamarock, and J. B. Klemp, 1997: The resolution dependence of explicitly modeled convective systems. *Mon. Wea. Rev.,* **125,** 527–548, doi:10.1175/1520-0493(1997)125<0527:TRDOEM>2.0.CO;2.

Wilson, J. W., and R. D. Roberts, 2006: Summary of convective storm initiation and evolution during IHOP: Observational and modeling perspective. *Mon. Wea. Rev.,* **134,** 23–47, doi:10.1175/MWR3069.1.